bioRxiv preprint doi: https://doi.org/10.1101/2022.08.26.505417; this version posted August 26, 2022. The copyright holder for this preprint (which was not certified by peer review) is the author/funder. All rights reserved. No reuse allowed without permission.

Multiple polarity kinases inhibit phase separation of F-BAR protein Cdc15 and antagonize cytokinetic ring assembly in fission yeast

Rahul Bhattacharjee[1], Aaron Hall[2], MariaSanta C. Mangione[1,3], Maya G. Igarashi[1], Rachel H. Roberts-Galbraith[1,4], Jun-Song Chen[1], Dimitrios Vavylonis[2], and Kathleen L. Gould*

[1]Department of Cell and Developmental Biology, Vanderbilt University School of Medicine, Nashville, TN, USA

[2]Department of Physics, Lehigh University, 415 Lewis Lab, 16 Memorial Drive East, Bethlehem PA, USA

[3]Current address: Department of Internal Medicine, University of Texas Health Sciences Center, Dallas, TX 75390-9030

[4]Current address: Department of Cellular Biology, University of Georgia, GA, 30602, USA

*Author for correspondence: kathy.gould@vanderbilt.edu

Keywords: cytokinesis, fission yeast, F-BAR protein, intrinsically disordered region, protein kinases, paxillin, liquid-liquid phase separation

Abbreviations: cytokinetic ring, CR; plasma membrane, PM; intrinsically disordered region, IDR; mNeonGreen, mNG; spindle pole body, SPB; mCherry, mCh; brightfield, BF; liquid-liquid phase separation, LLPS

bioRxiv preprint doi: https://doi.org/10.1101/2022.08.26.505417; this version posted August 26, 2022. The copyright holder for this preprint (which was not certified by peer review) is the author/funder. All rights reserved. No reuse allowed without permission.

Abstract

The F-BAR protein Cdc15 is essential for cytokinesis in *Schizosaccharomyces pombe* and it plays a key role in attaching the cytokinetic ring (CR) to the plasma membrane. Cdc15's abilities to bind to the membrane and oligomerize via its F-BAR domain are inhibited by phosphorylation of its intrinsically disordered region (IDR). Multiple cell polarity kinases regulate Cdc15 IDR phosphostate, and of these the DYRK kinase Pom1 phosphorylation sites on Cdc15 have been shown in vivo to prevent CR formation at cell tips. Here, we compared the ability of Pom1 to control of Cdc15 phosphostate and cortical localization to that of other Cdc15 kinases: Kin1, Pck1, and Shk1. We identified distinct but overlapping cohorts of Cdc15 phosphorylation sites targeted by each kinase, and the number of sites correlated with each kinases' abilities to influence Cdc15 PM localization. Coarse-grained simulations predicted that cumulative IDR phosphorylation moves the IDRs of a dimer apart and toward the F-BAR tips. Further, simulations indicated that the overall negative charge of phosphorylation masks positively charged amino acids necessary for F-BAR oligomerization and membrane interaction. Finally, simulations suggested that dephosphorylated Cdc15 undergoes phase separation driven by IDR interactions. Indeed, dephosphorylated but not phosphorylated Cdc15 undergoes liquid-liquid phase separation to form droplets in vitro that recruit Cdc15 binding partners. In cells, Cdc15 phosphomutants also formed PM-bound condensates that recruit other CR components. Together, we propose that a threshold of Cdc15 phosphorylation by assorted kinases prevents Cdc15 condensation on the PM and antagonizes CR assembly.

bioRxiv preprint doi: https://doi.org/10.1101/2022.08.26.505417; this version posted August 26, 2022. The copyright holder for this preprint (which was not certified by peer review) is the author/funder. All rights reserved. No reuse allowed without permission.

Introduction

Cytokinesis is the final step in the cell division cycle that is achieved in many eukaryotes by employing an actin- and myosin-based cytokinetic ring (CR). CR assembly, constriction, and disassembly are each regulated and coordinated with other cell cycle events to protect genome integrity. Throughout cell division, the CR remains attached to the plasma membrane (PM) so that CR constriction results in PM opposition, fusion, and ultimately the physical separation of two daughter cells.

In the fission yeast *Schizosaccharomyces pombe,* the CR comprises approximately 40 proteins, including PM-bound scaffolds. One of these PM-binding proteins is the essential F-BAR protein Cdc15. Cdc15 is one of the first and most abundant components detected at the CR (Nurse *et al.*, 1976; Fankhauser *et al.*, 1995; Wu *et al.*, 2003; Wu and Pollard, 2005). An N-terminal F-BAR domain oligomerizes, binds membranes, and binds the formin Cdc12 and the paxillin-related Pxl1 (Carnahan and Gould, 2003; McDonald *et al.*, 2015; Willet *et al.*, 2015a; Snider *et al.*, 2020; Snider *et al.*, 2022). A C-terminal SH3 domain binds multiple CR components including the C2 domain protein Fic1 and Pxl1 (at a second binding site (Roberts-Galbraith *et al.*, 2009; Cortes *et al.*, 2015; Ren *et al.*, 2015; Martin-Garcia *et al.*, 2018; Bhattacharjee *et al.*, 2020). Between the F-BAR and SH3 domains is a long stretch of amino acids predicted to form an intrinsically disordered region (IDR) essential for Cdc15 function (Mangione *et al.*, 2019). Reducing the amount of Cdc15, preventing Cdc15 membrane binding and/or oligomerization, or deleting the Cdc15 SH3 domain destabilizes the CR during anaphase and leads to cytokinesis failure (Roberts-Galbraith *et al.*, 2009; Arasada and Pollard, 2011; McDonald *et al.*, 2015).

bioRxiv preprint doi: https://doi.org/10.1101/2022.08.26.505417; this version posted August 26, 2022. The copyright holder for this preprint (which was not certified by peer review) is the author/funder. All rights reserved. No reuse allowed without permission.

Cdc15 functions are regulated by its phosphostate (Fankhauser *et al.*, 1995; Roberts-Galbraith and Gould, 2010; Bhattacharjee *et al.*, 2020). During interphase, Cdc15 is primarily cytosolic and hyperphosphorylated (≥35 phosphorylation sites). Dephosphorylation of Cdc15 at mitotic onset is accompanied by its re-localization to the medial cortex, oligomerization, and interaction with protein partners.

Three distinct polarity kinases (DYRK kinase Pom1, MARK/PAR-1 kinase Kin1, and p21-activated kinase Pak1/Shk1/Orb2) are implicated in regulating Cdc15 phosphostatus in vivo and are capable of phosphorylating Cdc15 directly in vitro (Kettenbach *et al.*, 2015; Lee *et al.*, 2018; Bhattacharjee *et al.*, 2020; Magliozzi *et al.*, 2020). The effect of Pom1 phosphorylation on Cdc15 is the best understood. Concentrated at the cortex of growing cell ends, Pom1 signals to antagonize CR formation and septation at cell tips (Celton-Morizur *et al.*, 2006; Padte *et al.*, 2006; Huang *et al.*, 2007; Martin and Berthelot-Grosjean, 2009; Hachet *et al.*, 2011; Bhatia *et al.*, 2014) in part by phosphorylating Cdc15 and blocking Cdc15's ability to bind membrane and Pxl1 (Bhattacharjee *et al.*, 2020). Considerably less is known about how Kin1 and Shk1 influence Cdc15, and it is not understood why three distinct polarity kinases would be used to modulate Cdc15 function. One possibility is that each kinase regulates different aspects of Cdc15 function since they are reported to phosphorylate largely non-overlapping sites (Kettenbach *et al.*, 2015; Lee *et al.*, 2018; Magliozzi *et al.*, 2020). Alternatively, the three kinases may modulate Cdc15's properties similarly but each kinase is deployed with different spatial and temporal specificity. This idea is consistent with the distinct but overlapping localizations of Pom1, Kin1, and Shk1 at cell

bioRxiv preprint doi: https://doi.org/10.1101/2022.08.26.505417; this version posted August 26, 2022. The copyright holder for this preprint (which was not certified by peer review) is the author/funder. All rights reserved. No reuse allowed without permission.

tips and the CR (Huang *et al.*, 2007; Hachet and Simanis, 2008; Bhatia *et al.*, 2014; Lee *et al.*, 2018; Magliozzi *et al.*, 2020).

To dissect the importance of deploying multiple kinases to regulate Cdc15, we determined the individual contributions of Pom1, Kin1 and Shk1. We established that the cohort of sites phosphorylated by each kinase overlaps and discovered that a fourth kinase, protein kinase C Pck1, modulates Cdc15 phosphostate in vivo and phosphorylates Cdc15 directly in vitro. All four kinases affected Cdc15 membrane localization in a manner that correlated with the number of targeted phosphorylation sites. Coarse grain molecular dynamics simulations indicated that phosphorylation impacts the organization of the IDRs relative to the F-BAR domain within a dimer, with increasing phosphorylation promoting separation of the two IDRs and their clustering around F-BAR domain tips. Simulations also suggested that dephosphorylation might promote IDR-mediated liquid-liquid phase separation (LLPS). Using in vitro biochemical assays, we confirmed that IDR phosphorylation state governed Cdc15's ability to form droplets and recruit binding partners into them. In accord with the in vitro studies, Cdc15 phosphomutants formed cortical condensates that recruited other CR components within cells. Overall, our data indicate that Cdc15 condenses on the membrane and scaffolds CR components, and this function is controlled by limiting Cdc15 phosphorylation with spatiotemporal precision.

Results

Multiple polarity kinases modulate Cdc15 phosphostatus

bioRxiv preprint doi: https://doi.org/10.1101/2022.08.26.505417; this version posted August 26, 2022. The copyright holder for this preprint (which was not certified by peer review) is the author/funder. All rights reserved. No reuse allowed without permission.

When examined by SDS-PAGE and immunoblotting, the phosphorylated forms of Cdc15 migrate slowly and heterogeneously to generate a broad band that can be collapsed to a single band by phosphatase treatment (Figure 1A). Despite the many sites Pom1 targets in vitro (22) (Kettenbach *et al.*, 2015; Bhattacharjee *et al.*, 2020), we observed only a modest change in Cdc15 SDS-PAGE mobility in *pom1*Δ cells (Bhattacharjee *et al.*, 2020). Kin1 also phosphorylates Cdc15 (Kettenbach *et al.*, 2015; Lee *et al.*, 2018), so we tested whether inactivating Kin1 alone or in combination with Pom1 resulted in a more substantial change in Cdc15 phosphostate. To do this, we used *pom1*(T778G) (*pom1*^{as1}) (Padte *et al.*, 2006) and *kin1*(F220G) (*kin1*^{as1}) (Cadou *et al.*, 2010; Lee *et al.*, 2018) to inhibit Pom1 and Kin1 kinase activity, using the ATP analogue 3MB-PP1. We observed small increases in Cdc15 SDS-PAGE mobility when either kinase was individually inhibited and an additive increase when both kinases were inhibited (Figure 1B). However, this increase of mobility did not match the extent of dephosphorylation observed for the Pom1 site mutant, Cdc15-22A (Figure 1B). To rule out that inhibitor treatment of the *kin1*^{as1} mutant was unable to abrogate Kin1 activity, we examined Cdc15 phosphorylation state in *kin1*Δ compared to *cdc15-22A*. Again, we found modest change in Cdc15 mobility in *kin1*Δ cells (Figure 1C). We also found that Kin1 loss did not significantly change the migration of Cdc15-22A, which as we showed previously is still phosphorylated (Figure 1C) (Bhattacharjee *et al.*, 2020). These results indicate that many Cdc15 phosphosites remain modified in the absence of Pom1 and Kin1 function.

The p21-activated kinase Pak1/Shk1/Orb2 is a third polarity kinase that phosphorylates Cdc15 (Magliozzi *et al.*, 2020). Thus, we examined how inhibiting Shk1

bioRxiv preprint doi: https://doi.org/10.1101/2022.08.26.505417; this version posted August 26, 2022. The copyright holder for this preprint (which was not certified by peer review) is the author/funder. All rights reserved. No reuse allowed without permission.

alone or in combination with Pom1 and Kin1 affected Cdc15 phosphostate. For this, we used the ATP analog 3BrB-PP1-sensitive *shk1*^{as2} (M460A) (Cipak *et al.*, 2011; Magliozzi *et al.*, 2020) or temperature-sensitive *orb2-34* alleles (Verde *et al.*, 1995). We found that in both cases Shk1 inhibition modestly decreased Cdc15 phosphorylation (Figure 1D and E). Larger reductions in Cdc15 phosphorylation were observed when both Shk1 and Pom1, or Shk1 and Kin1 were inhibited (Figure 1F). A still larger decrease in Cdc15 phosphorylation was observed when all three polarity kinases were inhibited; however, Cdc15 remained phosphorylated and more phosphorylated than Pom1-resistant Cdc15-22A (Figure 1F). Taken together, these results indicate that still other kinases phosphorylate Cdc15.

To identify additional Cdc15 regulators, we screened all non-essential protein kinases known to participate in polarity or cell division and we found that Cdc15 phosphostatus was reduced in *pck1*Δ cells (Figure 1G). Pck1 is one of two protein kinase C enzymes in *S. pombe*; it acts downstream of Rho1 GTPase to regulate septum deposition and participates in the cell wall integrity pathway (Toda *et al.*, 1993; Kobori *et al.*, 1994; Arellano *et al.*, 1999; Sanchez-Mir *et al.*, 2014). Cdc15 phosphorylation was also modestly reduced by inhibiting the analog 3BrB-PP1 sensitive *pck1*^{as2} (M744G) mutant (Bohnert *et al.*, 2020) (Figure 1H). We next combined *pck1*^{as2} with the other three analog-sensitive mutations. When all four kinases were simultaneously inhibited, Cdc15 SDS-mobility approached that of Cdc15-22A (Figure 1I). While phosphatase treatment of Cdc15-22A revealed residual phosphorylation (Figure 1I), it appeared that Pom1, Kin1, Shk1 and Pck1 are together responsible for the bulk of Cdc15 phosphorylation.

bioRxiv preprint doi: https://doi.org/10.1101/2022.08.26.505417; this version posted August 26, 2022. The copyright holder for this preprint (which was not certified by peer review) is the author/funder. All rights reserved. No reuse allowed without permission.

Polarity kinases phosphorylate Cdc15 on shared and distinct sites

We performed in vitro assays to confirm that Cdc15 can be directly phosphorylated by Pck1, and to localize and compare the phosphorylation sites of these four protein kinases (Figure 1-figure supplement 1A). Kin1 was proposed to phosphorylate Cdc15 on sites distinct from those targeted by Pom1 (Kettenbach *et al.*, 2015; Lee *et al.*, 2018) and concordant with this finding, Kin1 phosphorylated Cdc15C (amino acids 441-927) but not Cdc15N (amino acids 1-460), whereas Pom1 is able to phosphorylate both fragments (Bhattacharjee *et al.*, 2020). Shk1 and Pck1 also phosphorylated Cdc15C but not Cdc15N (Figure 1-figure supplement 1A). Substituting the Pom1 phosphorylation sites in Cdc15C (Bhattacharjee *et al.*, 2020) with alanines (Cdc15-19A) or aspartic acids (Cdc15-19D) did not preclude phosphorylation by Kin1, Shk1 or Pck1 (Figure 1-figure supplement 1B)(also see Figure 3A) consistent with the idea that Shk1, Kin1, and Pck1 each phosphorylate Cdc15 at some distinct sites.

To test more deliberately whether any of these kinases influence Cdc15 phosphorylation by the others and whether they phosphorylate different sites, we carried out assays with each kinase in the presence of unlabeled ATP, removed the first kinase and then asked whether any of the other three kinases could phosphorylate pre-treated Cdc15C (Figure 2). We found reduced phosphorylation of Cdc15C by Shk1 and Pck1 after pre-phosphorylation by Pom1 (Figure 2A). When Shk1 was used as the first kinase, there was reduced Cdc15 phosphorylation by Pom1, Kin1, and Pck1 (Figure 2B). Cdc15C pre-phosphorylated by either Kin1 or Pck1 showed reduced phosphorylation by Pom1 or Shk1 (Figure 2C and D). However, when Cdc15C was phosphorylated by Kin1 first, it did not affect subsequent phosphorylation by Pck1, or

bioRxiv preprint doi: https://doi.org/10.1101/2022.08.26.505417; this version posted August 26, 2022. The copyright holder for this preprint (which was not certified by peer review) is the author/funder. All rights reserved. No reuse allowed without permission.

vice versa (Figure 2C and D). Taken together, our findings indicate that there is a complex pattern of Cdc15 phosphorylation by these four kinases with both shared and unique sites.

To define the exact phosphorylation sites that can be targeted by each kinase, we used a combination of mass spectrometry and tryptic phosphopeptide mapping. In contrast to Pom1, which phosphorylates 22 sites on Cdc15 in vitro (Bhattacharjee *et al.*, 2020), Kin1 and Shk1 phosphorylated 5 and 11 sites, respectively, all within the IDR (Figure 3A and Figure 3-figure supplement 1 and 2). Pck1 appeared to have a single major site of phosphorylation (S668) (Figure 3A and Figure 3-figure supplement 3). Validating the assignment of these sites, Kin1, Shk1 and Pck1 were unable to phosphorylate Cdc15C in which the relevant identified phosphorylation sites had been substituted with alanines (Figure 3B, C and D). A comparison of the sites phosphorylated by each of the four polarity kinases in vitro led us to conclude that multiple sites are shared among the kinases, although three kinases also phosphorylate unique sites consistent with previous data (Figure 3A) (Kettenbach *et al.*, 2015; Lee *et al.*, 2018; Magliozzi *et al.*, 2020).

Cdc15 mutants that prevent phosphorylation at sites targeted by polarity kinases localize more to the CR and alter cytokinesis timing

To evaluate the role of Cdc15 phosphorylation by the polarity kinases, we mutated the identified residues to alanine (to abolish phosphorylation) and integrated the series of phosphomutant alleles at the endogenous *cdc15* locus with or without an N-terminal mNeonGreen (mNG) tag. We chose not to generate asparate mutants because we previously found that they neither recapitulate the phosphorylated protein in

bioRxiv preprint doi: https://doi.org/10.1101/2022.08.26.505417; this version posted August 26, 2022. The copyright holder for this preprint (which was not certified by peer review) is the author/funder. All rights reserved. No reuse allowed without permission.

charge nor retain the ability to bind 14-3-3 proteins (Roberts-Galbraith and Gould, 2010), as is typical for S/T to D mutants (Dephoure *et al.*, 2013). Consistent with results from inhibiting all polarity kinases (Figure 1), replacing the complement of 31 phosphorylation sites in Cdc15 identified above with alanine led to a significant increase in Cdc15's electrophoretic mobility (Figure 3E). While phosphatase treatment of the Cdc15-31A mutant revealed that it is still phosphorylated (Figure 3E), the majority of wildtype Cdc15 is never so dephosphorylated, even during mitosis and cytokinesis (Figure 3F).

We next examined the effect of preventing phosphorylation on Cdc15 localization during cytokinesis. We found that there was more Cdc15-31A compared to Cdc15 in both the fully formed pre-constriction CR and in partially constricted CRs (Figure 4A) although the whole cell fluorescence intensities of wildtype and *cdc15-31A* cells were comparable (Figure 4B). We also found more Rlc1, the regulatory light chain of myosin II, in CRs of *cdc15-31A* cells relative to wildtype cells (Figure 4C), indicating that the additional Cdc15-31A recruited more myosin II into CRs. Time-lapse imaging with Rlc1-mNG and Sid4-mNG as markers of the CR and spindle pole body (SPB), respectively, showed that *cdc15*-31A cells had altered cytokinesis dynamics. Although the length of CR formation (cytokinetic node appearance to complete ring) was similar in wildtype and *cdc15-31A*, the periods of maturation (interval between CR formation and constriction initiation) and constriction (start to end of CR diameter decrease) were shorter in *cdc15-31A* (Figure 4D and E), in accord with the increased level of myosin II in the CR (Calvert *et al.*, 2011).

Kin1, Shk1, and Pck1 kinases inhibit Cdc15 membrane localization

bioRxiv preprint doi: https://doi.org/10.1101/2022.08.26.505417; this version posted August 26, 2022. The copyright holder for this preprint (which was not certified by peer review) is the author/funder. All rights reserved. No reuse allowed without permission.

Our finding of increased Cdc15-31A in the CR was consistent with previous findings that Pom1-mediated Cdc15 phosphorylation inhibits its PM localization as part of a mechanism Pom1 uses to prevent CR formation and septation at cell tips (Bhattacharjee *et al.*, 2020). Therefore, we reasoned that if Kin1, Shk1, or Pck1 were inhibited during interphase, Cdc15, which is primarily hyperphosphorylated and cytosolic at this stage, would change its cellular localization. To test this, we examined the spatial distribution of mNG-Cdc15 in each of the analog-sensitive mutants of the four kinases individually, or in combination, in interphase cells that do not contain CRs. The ratio of mNG-Cdc15 PM to cytoplasmic localization increased when any of the kinases was inhibited and was highest in the strain in which Pom1, Shk1 and Kin1 activities were all inhibited (Figures 5A and Figure 5-figure supplement 1A). Like Pom1, Shk1 and Kin1 also play roles in preventing tip septation when the positive cue for medial septation, Mid1, is missing (Cadou *et al.*, 2010; Magliozzi *et al.*, 2020) and we found that inhibition of Pck1 also allowed a small increase in tip septation in a *mid1*Δ background (Figure 5-figure supplement 2A). The percentage of tip septa formed when either Kin1^{as1}, Shk1^{as}, or Pck1^{as2} were inhibited in *mid1Δ* cells correlated with the extent of increased membrane localization (Figure 5-figure supplement 2A).

Because the ratio of PM to cytoplasmic localization of interphase cells appeared to increase as a function of the number of Cdc15 sites phosphorylated by each kinase (Figure 5A), we next examined the localization of the mNG-Cdc15 phosphomutants. Paralleling the results of kinase inhibition, we found that the percentage of cortical Cdc15 localization increased with the number of phosphosites mutated to alanine, with a significant jump between the 11A and the 22A mutants (Figures 5B and Figure 5-

bioRxiv preprint doi: https://doi.org/10.1101/2022.08.26.505417; this version posted August 26, 2022. The copyright holder for this preprint (which was not certified by peer review) is the author/funder. All rights reserved. No reuse allowed without permission.

figure supplement 1B). These results are also concordant with finding more Cdc15-31A in the CR (Figure 4A).

The significant increase in cortical localization between 11A and 22A mutations (Figure 5B) prompted us to investigate the intracellular localization of a different set of Cdc15 phosphomutants during interphase (Roberts-Galbraith and Gould, 2010). These initial mutants were tagged with GFP at their C-termini. While the results cannot be compared directly to the mNG, N-terminally tagged mutants, we again observed a significant increase in cortical localization in the 27A mutant compared to the 11A, 13A, or 18A mutants (Figure 5C). Inspection of the phosphorylation sites mutated in each of the mutants did not indicate that loss of specific sites or lack of phosphorylation of any specific IDR region correlated with the greatest localization change. Instead, the analysis suggested that a threshold of dephosphorylation may trigger a change in protein conformation and ability to bind membrane. We used modeling to explore this hypothesis.

Simulation of phospho-regulated Cdc15 conformational changes

To better understand how IDR phosphorylation regulates Cdc15, we performed coarse-grained molecular dynamics simulations in which each amino acid is represented by a single bead on the α carbon location while the solvent is represented implicitly. Interactions between beads were given by the Hydrophobicity Scale (HPS) model, developed to match the radius of gyration (R_G) for multiple IDRs (Dignon *et al.*, 2018), based on the Kapcha-Rossky hydropathy scale (Kapcha and Rossky, 2014). We further used an extension of the HPS model that includes the effects of phosphorylation

bioRxiv preprint doi: https://doi.org/10.1101/2022.08.26.505417; this version posted August 26, 2022. The copyright holder for this preprint (which was not certified by peer review) is the author/funder. All rights reserved. No reuse allowed without permission.

and associated change in charge interactions (Perdikari *et al.*, 2021). In our Cdc15 dimer model, the folded F-BAR and SH3 domains were fixed rigidly according to the recently determined crystal structure of the Cdc15 F-BAR domain [PDB 6XJ1;(Snider *et al.*, 2020)] and the AlphaFold model of the Cdc15 SH3 domain [AF-Q09822-F1; (Jumper *et al.*, 2021; Varadi *et al.*, 2022)]. All other amino acids were connected by flexible linkers with equilibrium length 3.81 Å (Figure 6A). Assuming HPS interactions between all beads in the system, we simulated Cdc15 dimers in different phosphorylation states: dephosphorylated, phosphorylated at all 31 sites on each IDR in the dimer, and at the sites for the individual kinases Kin1 (5 sites), Shk1 (11 sites), and Pom1 (22 sites). To check that the system approaches the same equilibrium, independent of the starting configuration, we performed simulations where IDRs were initially separated or where IDRs were initially interacting with each other (Figure 6A, Figure 6-figure supplement 1A and B).

Simulations showed that increasing phosphorylation drives a large structural transition in the Cdc15 dimer. In the dephosphorylated state, the IDRs preferred to interact with each other but progressive phosphorylation weakens this preference and drives the IDRs to the poles of the F-BAR (Figure 6B, Videos 1 and 2). Furthermore, simulations suggest the IDR makes contacts with F-BAR tips (Figures 6-figure supplement 2, figure supplement 3A). Although separation of the IDRs with increasing phosphorylation is gradual, visual inspection shows it begins to occur when the distance between the IDR center of mass (COM) of each chain exceeds 100 Å (Figure 6-figure supplement 1C). Furthermore, we see a significant increase in the fraction of time the IDRs spend with high COM separation for the Pom1 and fully phosphorylated cases

bioRxiv preprint doi: https://doi.org/10.1101/2022.08.26.505417; this version posted August 26, 2022. The copyright holder for this preprint (which was not certified by peer review) is the author/funder. All rights reserved. No reuse allowed without permission.

(Figure 6C, D). Additionally, we observe that the SH3 domains make contacts with the F-BAR domain in similar regions to the IDR, and these contacts are also regulated by phosphorylation (Figure 6- figure supplement 2 and figure supplement 3B). These simulation results suggest that phosphorylation inhibits Cdc15 by driving the IDR and SH3 regions towards the tips of the F-BAR domain, potentially blocking its end-to-end oligomerization and weakening PM avidity.

We repeated the Cdc15 dimer simulations using a different α carbon coarse-grained model previously applied to IDRs (Dignon *et al.*, 2018): the Kim and Hummer model D (KH D) (Kim *et al.*, 2008) based on the Miyazawa-Jernigan potential (Miyazawa and Jernigan, 1996) (see Methods). The trends revealed by the HPS model were confirmed, however the transitions between low and high IDR COM separation were more abrupt (Figure 6-figure supplement 1D and F). Unlike the HPS case, the systems did not fully equilibrate over comparable timescales, retaining memory of their separated or interacting starting IDR configurations (see Discussion).

To investigate how phosphorylation regulates the expansion of the Cdc15 IDR, we performed coarse-grained molecular dynamics simulations of the Cdc15 IDR (residues 327-854) in isolation. For the HPS model, dephosphorylated Cdc15 IDR is relatively collapsed and undergoes progressive expansion with increased phosphorylation, which is more pronounced for the Pom1 and fully phosphorylated cases (Figure 6E and F). In simulations which show the coil to globule transition with increasing temperature, we found that the phosphorylation-induced relative change in R_G is maximal near room temperature (Figure 6-figure supplement 4A and B). Similar results were obtained with the KH D model, although the change in IDR size was

bioRxiv preprint doi: https://doi.org/10.1101/2022.08.26.505417; this version posted August 26, 2022. The copyright holder for this preprint (which was not certified by peer review) is the author/funder. All rights reserved. No reuse allowed without permission.

smaller and the coil-to-globule transition happened at higher temperatures compared to HPS (Figure 6-figure supplement 5C and D). In order to determine the effect of the phosphorylation charge on these results, we simulated the fully phosphorylated case with -1.5e charge per phosphorylation, instead of -2e, for both models (the average value can vary between -1e and -2e at neutral pH based on the residues measured pKa values (Bienkiewicz and Lumb, 1999)). The expansion is commensurate with net charge added by phosphorylation (Figure 6F, Figure 6-figure supplement 5), in agreement with the diagram of states of (Das and Pappu, 2013) that predicts an increase in negative charge due to phosphorylation would cause the Cdc15 IDR to transition from a collapsed globule or tadpole closer to a random coil, hairpin or chimera (Figure 6-figure supplement 5).

Cdc15 IDR undergoes phosphoregulated phase separation

The collapse of the dephosphorylated IDRs into a medial globule in our dimer simulations and the relatively compact size of the single dephosphorylated IDR simulations, suggest the possibility that the dephosphorylated Cdc15 IDR regions undergo phase separation with other Cdc15 dimers and/or other CR proteins. Indeed, a reduction of R_G, is a good indicator of intrinsically disordered protein tendency to phase-separate (Lin and Chan, 2017). Increasing phosphorylation of the Cdc15 IDR phosphorylation might disrupt phase separation, similar to multisite phosphorylation of the low sequence-complexity region of FUS (Monahan *et al.*, 2017).

To experimentally test whether Cdc15 IDR can undergo liquid-liquid phase separation (LLPS) regulated by IDR phosphorylation, we first expressed recombinant

bioRxiv preprint doi: https://doi.org/10.1101/2022.08.26.505417; this version posted August 26, 2022. The copyright holder for this preprint (which was not certified by peer review) is the author/funder. All rights reserved. No reuse allowed without permission.

Cdc15-IDR-SH3 (residues 327-927) together with Pom1 to ensure that the IDR became highly phosphorylated upon translation (Bhattacharjee *et al.*, 2020). In these first experiments, the F-BAR domain was omitted because of its propensity to oligomerize at physiological salt concentrations in vitro (McDonald *et al.*, 2015; Snider *et al.*, 2020). Cdc15 IDR-SH3 was purified at high salt concentration (Figure 7-figure supplementary 1A), labeled with Alexa Fluor-488, and treated with λ-phosphatase or buffer control (Figure 7-figure supplementary 1B). The salt concentration was reduced to 150 mM NaCl and a molecular crowding agent (5% PEG, see methods) was added in certain experiments, as indicated. Condensate formation was observed and measured by fluorescence microscopy. We found that Cdc15-IDR-SH3 formed droplets in a manner that depended on protein and salt concentrations (Figure 7A and B). Importantly, phase separation was observed only when Cdc15-IDR-SH3 was dephosphorylated (Figure 7A and B). Using the optimal protein concentration derived from phase diagrams (25 μM) (Figure 7A), we observed that Cdc15-IDR-SH3 droplets could fuse, consistent with a dynamic liquid-like nature (Figure 7C and Video 3). Fluorescence recovery after photobleaching (FRAP) analysis of Cdc15-IDR-SH3 droplets in the absence of PEG showed that the droplets were dynamic (Figure 7D). Furthermore, line-scans through the center of each droplet confirmed that dephosphorylated Cdc15-IDR-SH3 incorporated homogenously into the droplets (Figure 7E and F). We next tested whether the His-Cdc15-IDR-SH3 would phase separate on supported lipid bilayers. Similar to the in-solution results, dephosphorylated membrane-bound Cdc15-IDR-SH3 consistently formed condensates in a protein and salt concentration-dependent manner (Figure 7G and H).

bioRxiv preprint doi: https://doi.org/10.1101/2022.08.26.505417; this version posted August 26, 2022. The copyright holder for this preprint (which was not certified by peer review) is the author/funder. All rights reserved. No reuse allowed without permission.

Via its SH3 domain, Cdc15 binds Fic1 regardless of Cdc15 phosphostate and also paxillin-like Pxl1 when Cdc15 is dephosphorylated (Roberts-Galbraith *et al.*, 2009; Bhattacharjee *et al.*, 2020). The single PxxP motif in Pxl1 that binds the Cdc15 SH3 domain has been mapped and the interaction with Cdc15 SH3 recapitulated using a synthetic peptide consisting of Pxl1 residues 177-188 (Snider *et al.*, 2022). We sought to determine whether phase-separated droplets of dephosphorylated Cdc15-IDR-SH3 could recruit Pxl1 and Fic1. When Cdc15-IDR-SH3 was combined with equal concentrations of either Fic1 and/or the Pxl1 peptide, we observed droplets containing all the molecules only when Cdc15-IDR-SH3 was dephosphorylated (Figure 8A). We next asked whether full-length Cdc15 would also undergo LLPS in solution and for this we used an F-BAR oligomerization mutant (E30K, E152K) (Figure 8-figure supplement 1A) to prevent extensive F-BAR mediated oligomerization in vitro. In these assays, in addition to the Pxl1 peptide and Fic1 (Figure 8-figure supplement 1B), we also included a Cdc12 formin peptide (residues 20-40) that directly binds the Cdc15 F-BAR domain with high affinity (Willet *et al.*, 2015a). When we combined Cdc15 with Fic1 and the Pxl1 and Cdc12 peptides in equimolar ratio, we observed droplets containing multiple components but only when Cdc15 was dephosphorylated. With only three of the four components labeled, we observed that 84% of droplets contained at least three components (Cdc15, Fic1 and Pxl1 or Cdc15, Fic1, and Cdc12). The remainder of droplets contained either labeled Cdc15 and Fic1, Cdc15 and Pxl1 or Cdc15 and Cdc12 (Figure 8B and Figure 8-figure supplement 2). Therefore, we conclude that dephosphorylated Cdc15 can recruit its binding partners into phase-separated droplets.

bioRxiv preprint doi: https://doi.org/10.1101/2022.08.26.505417; this version posted August 26, 2022. The copyright holder for this preprint (which was not certified by peer review) is the author/funder. All rights reserved. No reuse allowed without permission.

Cdc15 condensates in cells exhibit liquid like properties

Our observations of dephosphorylated condensate formation in vitro was reminiscent of previous results showing that several different Cdc15 phosphoablating mutants localized in discrete puncta at the cortex of interphase cells (Roberts-Galbraith *et al.*, 2010; Bhattacharjee *et al.*, 2020), and wildtype Cdc15 in the CR has been observed to have a node-like organization by super-resolution imaging (Laplante *et al.*, 2016; McDonald *et al.*, 2017). Our new Cdc15 phosphomutants also formed cortical puncta or condensates during interphase, the number and size of which increased significantly in the 22A and 31A mutants (Figures 9A and B). We observed these condensates more closely and found that they were dynamic and underwent apparent fission and fusion events (Figure 9C, Videos 4 and 5), suggesting that they had some liquid-like properties. In *cdc15-31A* but not wildtype cells, Fic1 and Rlc1 were also recruited into these interphase condensates decorating the cortex (Figure 9D). Taken together, our data suggest that multisite phosphorylation of Cdc15 by polarity kinases inhibits Cdc15 condensate formation, Cdc15 membrane binding, and premature and non-medial CR construction.

Discussion

The F-BAR protein Cdc15 is an essential CR component and a linker of the CR to the PM. Cdc15 is phosphoregulated in a cell cycle specific manner, but how individual kinases contribute to this regulation and precisely how phosphorylation affects Cdc15 properties have not been clear. We presented evidence that progressive phosphorylation drives separation of the Cdc15 IDR regions, which antagonizes Cdc15

bioRxiv preprint doi: https://doi.org/10.1101/2022.08.26.505417; this version posted August 26, 2022. The copyright holder for this preprint (which was not certified by peer review) is the author/funder. All rights reserved. No reuse allowed without permission.

phase separation, condensate formation on the PM, and recruitment of other CR proteins. Leveraging a suite of Cdc15 protein kinases during interphase appears to ensure sufficient Cdc15 phosphorylation that CR assembly begins only at the proper place and time. More broadly, our work suggests phase separation as a mechanism involved in CR assembly.

The first detailed study of Cdc15 phosphorylation focused on phosphorylation sites that could be targeted by the Cdc14 family phosphatase, Clp1, and those matching a 14-3-3 binding site; this study estimated that ~35 sites within Cdc15 could be phosphorylated (Roberts-Galbraith *et al.*, 2010). Subsequently, several kinases have been identified to affect Cdc15 phosphostatus, and 74 sites of Cdc15 phosphorylation have been reported from MS-based studies (Chen *et al.*, 2013; Kettenbach *et al.*, 2015; Lee *et al.*, 2018; Swaffer *et al.*, 2018; Bhattacharjee *et al.*, 2020; Magliozzi *et al.*, 2020; Harris *et al.*, 2022). Based on gel shifts, the mutant generated in this study, Cdc15-31A, appears to be minimally phosphorylated compared to wild type protein. We reason therefore that the total number of Cdc15 phosphorylation sites is closer to 35 than 74 and that there are probably a number of mis-identified sites arising from the technical ambiguity of site assignment in peptides containing multiple potential phosphorylation sites. Indeed, there were numerous differences in the sites we identified for the polarity kinases compared to MS only-based studies. However, that Cdc15-31A retains some in vivo phosphorylation points to the existence of still another protein kinase(s) involved in Cdc15 phosphoregulation that contributes a unique set of targeted residues.

bioRxiv preprint doi: https://doi.org/10.1101/2022.08.26.505417; this version posted August 26, 2022. The copyright holder for this preprint (which was not certified by peer review) is the author/funder. All rights reserved. No reuse allowed without permission.

Given these technical challenges, it has been unclear exactly which Cdc15 sites each kinase phosphorylates and whether they affect the protein similarly. Our results indicate that there is little if any cooperativity or antagonism among the kinases and point to the total charge added or removed from the IDR as the most significant regulatory factor. The only specificity we found is the number of sites that can be phosphorylated by each kinase, assigned using a combination of technical approaches that is more accurate than an MS only-based approach. Our simulation results suggest that a certain threshold of phosphorylation must be reached to elicit a major change in IDR organization and IDR-IDR interaction, and we reason that there is an inherent limitation to how any single kinase can affect Cdc15 structure and function. This may explain why so many protein kinases are involved in Cdc15 phosphoregulation, particularly given its high intracellular concentration (Wu and Pollard, 2005). Pom1, Kin1, and Shk1 share additional substrates involved in cell division (Lee *et al.*, 2018; Magliozzi *et al.*, 2020), so they may control other CR components in concert with Cdc15 to maximally affect CR position and dynamics. Interestingly, while preventing Cdc15 phosphorylation with the Cdc15-31A mutant speeds up cytokinesis, consistent with more myosin II being recruited to the CR at an earlier time, our work demonstrates that re-phosphorylation of Cdc15 is not required for CR constriction or cell separation and that Cdc15 need not be removed from the membrane to allow cytokinesis to proceed. Rather, the phosphorylation of Cdc15 helps prevent incorrect division site placement.

We previously hypothesized that Cdc15's conformation was regulated by its phosphostate based on the observations that a site-specific protease cleaved only phosphorylated Cdc15, the phosphorylated and dephosphorylated forms behaved very

bioRxiv preprint doi: https://doi.org/10.1101/2022.08.26.505417; this version posted August 26, 2022. The copyright holder for this preprint (which was not certified by peer review) is the author/funder. All rights reserved. No reuse allowed without permission.

differently by analytical ultracentrifugation, and only dephosphorylated Cdc15 appeared filamentous by negative-stain EM (Roberts-Galbraith *et al.*, 2010). In this work, we studied Cdc15 conformation computationally using coarse grained molecular dynamics. While such methods lack the detail needed to predict local features such as secondary structure, they are well suited to address phenomena driven by thermodynamic forces representing averages over disordered configurations, such as in liquid-liquid phase separation, macromolecular crowding, and relationship between single chain systems and aggregate behaviors. All-atom simulations provide the highest molecular resolution but suffer from limited sampling when investigating IDR properties even when making use of state-of-the-art methods and computational resources (Shea *et al.*, 2021).

Our simulations demonstrate how Cdc15 undergoes a large conformational change upon changing levels of phosphorylation. This behavior reflects the tunability of its IDR, the amino acid sequence of which places it at a transition point between a collapsed globule and an expanded coil. The large size of the IDR and number of phosphorylation sites together with our results using two different coarse-grained potentials (HPS and KH D) indicate that this large reorganization of the IDR is a robust phenomenon. The sharpness of the predicted transition as a function of degree of phosphorylation, however, may depend on uncertainties in coarse grained interaction potentials: the models used here have not been tuned to reproduce IDR-globular interactions and considered IDRs less than 300 amino acids long, while the Cdc15 IDR is greater than 500 amino acids long. In the HPS model, the stronger pairwise interaction between the IDR and globular region assists in bringing the IDRs together, while the pairwise interactions weakened in the KH D model by SASA scaling leads to

bioRxiv preprint doi: https://doi.org/10.1101/2022.08.26.505417; this version posted August 26, 2022. The copyright holder for this preprint (which was not certified by peer review) is the author/funder. All rights reserved. No reuse allowed without permission.

weaker IDR-globular interactions and a more abrupt transition (reflected in KH D simulations that are harder to equilibrate). While our simulations have refined our understanding of phospho-regulated Cdc15 conformational changes, other binding interactions of dephosphorylated Cdc15, such as with formin Cdc12, Pxl1 and calcineurin, or itself upon oligomerization (McDonald *et al.*, 2015; Willet *et al.*, 2015a; Mangione *et al.*, 2019; Bhattacharjee *et al.*, 2020; Snider *et al.*, 2020) may extend or reinforce the conformational changes predicted by simulations of the Cdc15 dimer alone.

Similar to Cdc15 condensation into droplets in vitro, Cdc15 alanine phosphomutants and Cdc15 in strains subjected to kinase inhibition form cortical condensates in vivo, the number and size of which are controlled by the extent of Cdc15 phosphorylation. These puncta also exhibit some liquid-like properties, apparently undergoing fusion and fission events. Further, we observed here and previously (Roberts-Galbraith and Gould, 2010) that Cdc15 cortical condensates recruit other CR components, and within the CR, Cdc15 has been observed in node-like structures by super-resolution imaging (Laplante *et al.*, 2016; McDonald *et al.*, 2017). Taken together, these observations suggest that CR assembly involves condensation of a key membrane-bound scaffold, analogous to what occurs at other actin-based structures such as sites of endocytosis in yeast and focal adhesions in higher eukaryotes (Day *et al.*, 2021; Case *et al.*, 2022; Kozak and Kaksonen, 2022).

In wildtype cells, CRs form from cortical cytokinetic nodes that coalesce into the CR (Balasubramanian *et al.*, 2004; Pollard and Wu, 2010; Willet *et al.*, 2015b; Rincon

bioRxiv preprint doi: https://doi.org/10.1101/2022.08.26.505417; this version posted August 26, 2022. The copyright holder for this preprint (which was not certified by peer review) is the author/funder. All rights reserved. No reuse allowed without permission.

and Paoletti, 2016; Pollard and O'Shaughnessy, 2019). Cytokinetic node assembly begins with the anillin-related protein Mid1 arriving at the cortex and becoming stably anchored there (Wu *et al.*, 2003; Wu *et al.*, 2006; Clifford *et al.*, 2008; Coffman *et al.*, 2009; Laporte *et al.*, 2011; Akamatsu *et al.*, 2014). Then, other proteins including Cdc15 are recruited to Mid1 nodes (Laporte *et al.*, 2011). Like Cdc15, Mid1 contains a long IDR subject to multisite phosphorylation by a collection of kinases that control its localization (Bahler *et al.*, 1998; Paoletti and Chang, 2000; Rincon and Paoletti, 2012; Willet *et al.*, 2019{Almonacid, 2011 #108)} and the Mid1 N-terminus undergoes phase separation to form droplets in vitro (Chatterjee and Pollard, 2019). It was proposed that phase separation is not a major mechanism underlying Mid1 node formation because nodes contain fixed component ratios and have not been reported to undergo fusion or fission (Laplante *et al.*, 2016; Chatterjee and Pollard, 2019). However, Mid1 leaves the CR as it constricts (Wu *et al.*, 2003) and CRs can form in the absence of Mid1 (Chang *et al.*, 1996; Sohrmann *et al.*, 1996; Huang *et al.*, 2007). FRAP analyses indicate that there are both dynamic and immobile populations of Cdc15 in the CR (Clifford *et al.*, 2008; Roberts-Galbraith *et al.*, 2009; Roberts-Galbraith and Gould, 2010; Laporte *et al.*, 2011; McDonald *et al.*, 2015; Kamnev *et al.*, 2021). It is thus possible that initial Cdc15 condensates develop into more stable structures if assembled with Mid1 or other proteins.

Considering our results and the large number of proteins involved in cytokinetic nodes and the CR that involve IDRs with multiple phosphorylation sites, it is intriguing to speculate that phosphorylation pathways drive transitions in nanoscale organization of cytokinetic nodes and contractile ring anchoring by pushing the multi-component

bioRxiv preprint doi: https://doi.org/10.1101/2022.08.26.505417; this version posted August 26, 2022. The copyright holder for this preprint (which was not certified by peer review) is the author/funder. All rights reserved. No reuse allowed without permission.

cytokinesis system across condensation, demixing, or evaporation phase boundaries (Jacobs and Frenkel, 2017), with Cdc15 playing a central role. Interactions with charged lipids, lipid domains on the PM, as well as membrane curvature could also feed into these processes.

Acknowledgements

We are grateful to Nathan McDonald for advice on LLPS assays, Mohan Balasubramanian, Juraj Gregan, and Xavier Le Goff for providing strains, and Jitender Singh Bisht for performing the experiments shown in Figures 5A and Figure 5-figure supplement 1A. We thank Jeetain Mittal for providing feedback on the simulations and source code for the KH D model implemented in LAMMPS. Portions of this research were conducted on Lehigh University's Research Computing infrastructure partially supported by NSF Award 2019035 and the high-performance computing capabilities of the Extreme Science and Engineering Discovery Environment (XSEDE), supported by the National Science Foundation, project no. TG-MCB180021. M.C.M. was supported by NIH grants F31GM119252 and T32GM007347. This work was supported by NIH grant R35GM136372 to D.V. and NIH grant R35GM131799 to K.L.G.

Materials and Methods

Yeast methods

Table S1 lists *S. pombe* strains used in this study. Cells were cultured in rich medium YES with supplements or Edinburgh minimal media EMM plus selective supplements (Moreno *et al.*, 1991). To integrate *cdc15* mutants at the endogenous locus,

bioRxiv preprint doi: https://doi.org/10.1101/2022.08.26.505417; this version posted August 26, 2022. The copyright holder for this preprint (which was not certified by peer review) is the author/funder. All rights reserved. No reuse allowed without permission.

cdc15^{+}*/cdc15::ura4*$^{+}$ diploids were transformed with pIRT2-*cdc15* mutant constructs containing 5' and 3' noncoding flanks, sporulated, and *cdc15::ura4*$^{+}$ cells containing the plasmid were isolated on selective medium. Haploid integrants were then isolated based on resistance to 5-fluorourotic acid (5-FOA) (United States Biological; F5050) and integration of the *cdc15* mutations was verified by growth on selective media followed by PCR and DNA sequencing. *S. pombe* cells were transformed with a lithium acetate method or by electroporation (Keeney and Boeke, 1994; Gietz *et al.*, 1995). Introduction of tagged loci or *cdc15* mutants into other genetic backgrounds was accomplished using standard *S. pombe* mating, sporulation, and tetrad dissection techniques.

To inhibit Pom1^{as1} and Kin1^{as1} in vivo, cells were grown in YES at 32°C to mid-log phase and treated with 4-amino-1-tert-butyl-3-(3-methylbenzyl)pyrazolo[3,4-3]pyrimidine (3MB-PP1) (Toronto Research Chemical; A602960 or Cayman Chemical; 17860) at a final concentration of 15 μM for 30 min. Pck1^{as2} and Shk1^{as2} were inhibited with 30 μM 3-[(3-Bromophenyl) methyl]-1-(1,1-dimethylethyl)-1H-pyrazolo[3,4-d]pyrimidin-4-amine 4-amino-1-tert-butyl-3-(3-bromobenzyl)pyrazolo[3,4-d]pyrimidine (3BrB-PP1) (Abcam; ab143756) for 30 min. Both inhibitors (3MB-PP1 and 3BrB-PP1) were used at the above-mentioned concentrations to inhibit combinations of analog-sensitive kinase mutants. As control, cells were grown in equivalent concentration of DMSO (Sigma; D2650).

Denatured lysis and immunoprecipitation-phosphatase assays

bioRxiv preprint doi: https://doi.org/10.1101/2022.08.26.505417; this version posted August 26, 2022. The copyright holder for this preprint (which was not certified by peer review) is the author/funder. All rights reserved. No reuse allowed without permission.

Cell pellets (15 OD) were collected and snap frozen in dry ice-ethanol baths. Pellets were resuspended and washed once in 1 ml NP-40 buffer (6 mM Na_2HPO_4, 4 mM NaH_2PO_4, 1% NP-40, 150 mM NaCl, 2 mM EDTA, 50 mM NaF, 4 μg/mL leupeptin, 0.1 mM Na_3VO_4) with the addition of 1 mM PMSF (Sigma-Alrdrich; P7626), 2 mM benzamidine (Sigma-Alrdrich; B6506), and 0.5 mM diisopropyl fluorophosphate (Sigma-Aldrich; D0879-1G). Pellets were then lysed by bead disruption using a Fast-Prep instrument (MP Biomedicals) followed by denaturation by boiling at 95°C for 1 min with 300 μL SDS lysis buffer (10 mM $NaPO_4$, pH 7.0, 0.5% SDS, 1mM EDTA, 50 mM NaF, 100 μM Na_3VO_4) with 1 mM dithiothreitol (DTT) and 4 μg/ml leupeptin (Sigma Aldrich;L2884). Lysates were extracted by further addition of 800 μL of NP-40 buffer. After a clearing spin at 13,000 rpm for 5 min at 4°C, the supernatant was collected in a fresh tube and a small portion of the lysate was boiled with 5X SDS sample buffer for direct immunblotting. For immunoprecipitations, the remainders of the lysates were nutated with anti-Cdc15 polyclonal antibody (VU326) (Roberts-Galbraith *et al.*, 2009) for 1 hr at 4°C followed by incubation with protein A sepharose (GE Healthcare; 17-5280-04) for 30 min at 4°C. For phosphatase assays, the sepharose beads were washed two times with NP-40 buffer, two times with 1X phosphatase buffer (50 mM HEPES pH 7.4, 150 mM NaCl), and either incubated with buffer control or lambda protein phosphatase (λ) (New England Biolabs; P0753) according to the manufacturer's protocol. The reactions were stopped by the addition of gel sample buffer. Immunoblot analysis was performed as previously described (Roberts-Galbraith *et al.*, 2009). Briefly, to best visualize different Cdc15 phosphospecies, proteins were resolved by SDS-PAGE using freshly poured (within 24 hr) 8% Tris-glycine gels at 150 volts for 2.25 hr or pre-poured

bioRxiv preprint doi: https://doi.org/10.1101/2022.08.26.505417; this version posted August 26, 2022. The copyright holder for this preprint (which was not certified by peer review) is the author/funder. All rights reserved. No reuse allowed without permission.

NuPAGE 3-8% Tris-Acetate gel (Invitrogen; EA03752) for 2.15 hr (Figure 1C, D and H). Then, proteins were transferred to PVDF membrane (Immobilon FL; IPFL00010) for 2 hr. Anti-Cdc15 polyclonal antibody (VU326) or anti-α-tubulin monoclonal antibody (Sigma-Aldrich; B512) was used for immunoblotting. Secondary antibodies were conjugated to IRDye 680 or IRDye 800 (LI-COR Biosciences) and visualized using an Odyssey instrument (LI-COR Biosciences).

Recombinant protein purification

Bacteria were grown in Terrific Broth media (23.6g/L Yeast Extract, 11.8g/L tryptone, 9.4g/L K_2HPO_4, 2.2g/L KH_2PO_4, 4ml/L glycerol) with appropriate antibiotics to log-phase (OD_{595} 1-1.5) at 36°C. Cells were incubated on ice for 15 min and induction was initiated with the addition of 0.4 mM isopropyl β-D-1-thiogalactopyranoside (IPTG) (Fisher Scientific; BP1755). Proteins were produced for 16-18 hr at 18°C.

For MBP and GST fusion proteins, frozen cell pellets were lysed in either MBP buffer (20 mM Tris-HCl pH 7.4, 150 mM NaCl, 1 mM EDTA, 1 mM DTT) or GST buffer (4.3 mM $NaHPO_4$, 137 mM NaCl, 2.7 mM KCl, 1 mM DTT) with the addition of 200 µg/mL lysozyme (Sigma-Aldrich; L6876), cOmplete™ EDTA-free protease inhibitor cocktail (Roche; 05056489001), and 0.1% NP-40 (US Biologicals; N3500). Buffers were modified for MBP-Pxl1 to exclude EDTA. Continuous agitation on ice for 20 min was used to suspend the cell pellet. Then, lysates were sonicated three times for 30 s, with at least 30 s pause between sonications (Sonic Dismembrator Model F60, Fisher Scientific; power 15 watts). Lysates were cleared for 15-30 min at 10-13K rpm. Cleared lysate was then used in a batch purification protocol by addition of either amylose (New England Biolabs, Inc.; E8021L) or GST-bind (EMD Millipore; 70541) resin for 2 hr at

bioRxiv preprint doi: https://doi.org/10.1101/2022.08.26.505417; this version posted August 26, 2022. The copyright holder for this preprint (which was not certified by peer review) is the author/funder. All rights reserved. No reuse allowed without permission.

4°C. Then, resin was washed three times for 5 min at 4°C with the appropriate buffer. To elute proteins, resins were resuspended in an equal volume of appropriate elution buffer and nutated for 30 min at 4°C. MBP fusion proteins were eluted in MBP buffer supplemented with 10 mM maltose (Fisher Scientific; M75-100) and GST proteins were eluted in GST elution buffer (50 mM Tris-HCl pH 8, 10 mM glutathione (Sigma-Aldrich; G4251). The supernatant was separated from the resin to a fresh tube. Eluted fusion proteins were then aliquoted, snap frozen, and stored at -80°C. GST-Cdc15C-19A and 19D were made by mutating the Pom1 phosphorylation sites (T419, T492, S511, S527, S605, S636, S702, S710, S721, S732, S743, S752, S774, S785, S786, S813, S821, S831, S836, S840) to alanine or aspartic acid in the GST-Cdc15C vector (Bhattacharjee *et al.*, 2020).

To purify His_6-Cdc15-IDR-SH3 (residues 327-927) or His-Fic1, frozen cell pellets were lysed in buffer (50 mM Tris-HCl pH 7.4, 500 mM NaCl, 1 mM TCEP) with the addition of 200 µg/ml lysozyme (Sigma-Aldrich; L6876), cOmplete^{TM} EDTA-free protease inhibitor cocktail (Roche; 05056489001), and 0.1% NP-40 (US Biologicals; N3500). Then, lysates were sonicated three times for 30 s, with at least 30 s pause between sonications (Sonic Dismembrator Model F60, Fisher Scientific; power 15 watts). Lysates were cleared for 15-30 min at 10-13K rpm. Cleared lysate was then applied to His-Trap HP (1ml) (Cytiva; 17524701) using an AKTA pure system (Cytiva). Proteins bound to the column were eluted using freshly prepared buffer (50 mM Tris-HCl pH 7.4, 500 mM NaCl, 1 mM TCEP and 200 mM imidazole) and then concentrated using an Amicon Ultra 0.5 Centrifugal Unit (Milipore Sigma; UFC501096). Full length

bioRxiv preprint doi: https://doi.org/10.1101/2022.08.26.505417; this version posted August 26, 2022. The copyright holder for this preprint (which was not certified by peer review) is the author/funder. All rights reserved. No reuse allowed without permission.

Cdc15 oligomerization mutant (Cdc15-E30K, E152K) was prepared as described previously (Bhattacharjee *et al.*, 2020).

Protein concentration was calculated from either Coomassie Brilliant Blue G (Sigma-Aldrich; B0770) staining of SDS-PAGE-separated purified proteins and Bovine Serum Albumin (BSA) standards (Sigma-Aldrich; A2153) or by using a Nanodrop spectrophotometer (ND1000).

In vitro kinase assays

Radioactive in vitro kinase assays were performed in Kin1 buffer (50 mM Tris pH 7.5, 25 mM NaCl, 10 mM $MgCl_2$, 1 mM DTT, 200 µM ATP), Shk1 buffer (40 mM HEPES, pH 7.5, 10 mM $MgCl_2$ with 200 µM ATP) or Pck1 buffer (4 mM HEPES, pH 7.5, 5 mM $MgCl_2$, 2 mM DTT, 0.5 mM EGTA with 200 µM ATP) with 4 µCi γ-^{32}P-ATP (PerkinElmer BLU002250UC). For each 25 µL kinase reaction, 0.4 µg of kinase (MBP-Kin1 (amino acids 1-520,T299D), GST-Shk1 and MBP-Pck1 (amino acids 644-988,T823E) and 2 µg of substrate (MBP, MBP-Cdc15N (amino acids 1-405), MBP-Cdc15C (amino acids 441-927)) were used. After 30 min at 30°C, reactions were stopped with the addition of 10 µL 5X sample buffer, boiled and analyzed by SDS-PAGE. Inputs were detected by Coomassie Blue staining, and ^{32}P incorporation was detected by autoradiography.

For testing the effect of one kinase on the phosphorylation of Cdc15C by another, in vitro kinase assays were performed first with unlabeled ATP. The substrates (MBP-Cdc15C or GST-Cdc15C) were on beads and the kinases were in the supernatant. After the first kinase assay (30 min at 30°C), the beads were washed 3 times in 500 µL of the corresponding 1X kinase assay buffer to remove the kinase.

bioRxiv preprint doi: https://doi.org/10.1101/2022.08.26.505417; this version posted August 26, 2022. The copyright holder for this preprint (which was not certified by peer review) is the author/funder. All rights reserved. No reuse allowed without permission.

Bead-bound substrates (phosphorylated or not in the first reaction) were then divided into tubes and incubated with one of three kinases or buffer control in the presence of 4 µCi γ-^{32}P-ATP. All secondary kinase assays were performed in 25 µL total volume for 30 min at 30°C. These reactions were stopped with the addition of 10 µL 5X sample buffer, boiled for 2 min and analyzed by SDS-PAGE. Inputs were detected by Coomassie Blue staining, and ^{32}P incorporation was detected by autoradiography.

Kinase reactions for phosphopeptide mapping were performed with 0.2 ug of each kinase added to 2 ug substrates, GST-Cdc15C (amino acids 441-927) or GST-Cdc15C1 (amino acids 600-927) in its corresponding kinase assay buffers with 100 µM cold ATP, 4 µCi γ-^{32}P-ATP, and 10 mM $MgCl_2$ at 30°C for 30 min. Reactions were quenched by boiling in SDS-PAGE sample buffer.

Kinase assays for the identification of phosphorylation sites were performed with 200 µM unlabeled ATP, 1 µL of recombinant kinase and in 25 µL final volume. After a 15 min incubation with kinase, a second equal aliquot of kinase was added and the reaction stopped after and additional 45 min. In each case, 2 µg of GST-Cdc15C was used as substrate.

Phospho-peptide mapping

Phosphorylated proteins (GST-Cdc15C and GST-Cdc15C1) were resolved by SDS-PAGE, transferred to PVDF membranes, and visualized by autoradiography. Phosphopeptides were released from membrane slices with 10 µg trypsin at 37°C overnight with a second addition of 10 µg trypsin and incubation at 37°C the next day for 2 hr. Released peptides were lyophilized and resuspended in pH 1.9 buffer (Boyle *et al.*, 1991). Tryptic phosphopeptides were separated in the first dimension by thin-layer

bioRxiv preprint doi: https://doi.org/10.1101/2022.08.26.505417; this version posted August 26, 2022. The copyright holder for this preprint (which was not certified by peer review) is the author/funder. All rights reserved. No reuse allowed without permission.

electrophoresis and in the second dimension by chromatography (Boyle *et al.*, 1991). TLC plates were exposed to film for 2-4 d with intensifying screens.

Phosphorylation site identification by mass spectrometry

TCA-precipitated proteins were digested and analyzed by two-dimensional liquid chromatography/tandem mass spectrometry as described previously (Chen *et al.*, 2013), except that the following modifications were made. Proteins were digested by trypsin, chymotrypsin, and elastase. The number of salt elution steps was reduced to 6 (i.e., 0, 25, 50, 100, 600, 1000, and 5000 mM ammonium acetate). Peptide identifications were filtered and assembled using Scaffold (version 4.8.4; Proteome Software) and phosphorylation sites were analyzed using Scaffold PTM (version 3.1.0) using the following filters: minimum of 99% protein identification probability, minimum of five unique peptides, minimum of 95% peptide identification probability.

Microscopy and image analysis

Yeast for live-cell imaging were grown at 25°C. Live-cell images of *S. pombe* cells were acquired using a Zeiss Axio Observer inverted epifluorescence microscope with Zeiss 63X Oil (1.46 NA) and captured using Zeiss ZEN 3.0 (Blue edition) software. The acquisition setting for mNG-Cdc15 was set at 95% (intensity) and 600 ms (exposure time) with a Z-stack step size of 0.25 um and a total of 21 Z-slices.

Time-lapse imaging was performed on log-phase cells at 25°C using a Personal DeltaVision (Cytiva Life Sciences, Marlborough, MA) that includes a microscope (IX71; Olympus), 60 × NA 1.42 Plan Apochromat and 100 × NA 1.40 U Plan S Apochromat objectives, fixed and live-cell filter wheels, a camera (a pco.edge 4.2 sCMOS), and softWoRx imaging software (Leica). Time-lapse imaging was performed in YES media

bioRxiv preprint doi: https://doi.org/10.1101/2022.08.26.505417; this version posted August 26, 2022. The copyright holder for this preprint (which was not certified by peer review) is the author/funder. All rights reserved. No reuse allowed without permission.

in a CellASIC ONIX microfluidics perfusion system (Millipore Sigma, Burlington, MA). Cells were loaded into Y04C plates for 5 s at 8 psi, and YES liquid medium flowed into the chamber at 5 psi throughout the time-lapse. Images were acquired every 2 minutes with 0.5 µm optical spacing. Time-lapse images were deconvolved with 10 iterations and visualized as maximum projections.Images used for fluorescence quantification were not deconvolved.

TIRF images were recorded on a Personal DeltaVision (Cytiva Life Sciences, Marlborough, MA) that includes a microscope (IX71; Olympus), 60 × NA 1.42 Plan Apochromat and 100 × NA 1.40 U Plan S Apochromat objectives, fixed and live-cell filter wheels, a camera (a pco.edge 4.2 sCMOS), and softWoRx imaging software (Leica). The 488 laser was used for illumination of Alexa-488 labelled Cdc15-IDR-SH3.

Quantitative analysis of microscopy data was performed using Fiji (a version of ImageJ software available at https://fiji.sc) (Schindelin *et al.*, 2012). All quantifications were performed on non-deconvolved, sum projected images. For all intensity measurements, the background intensity was subtracted. The background intensity was found by taking a measurement in an area with no cells. The raw intensity of the background was divided by its area, which was multiplied by the area of the intensity measurement of interest. This number was subtracted from the raw integrated intensity of measurement of interest (Waters, 2009).

Quantification of mNG-Cdc15 PM to cytoplasmic ratio

The acquisition setting for mNG-Cdc15 was set at 95% (intensity) and 600 ms (exposure time) with a Z-stack step size of 0.25 um and a total of 21 Z-slices. We used two homemade scripts (macros) to quantify the ratio of mNG-Cdc15 on the PM to mNG-

bioRxiv preprint doi: https://doi.org/10.1101/2022.08.26.505417; this version posted August 26, 2022. The copyright holder for this preprint (which was not certified by peer review) is the author/funder. All rights reserved. No reuse allowed without permission.

Cdc15 in the cytoplasm of interphase cells. The first macro subtracts the background and stacks the image to prepare for the second macro. The second macro utilizes the "3D Object Counter" plugin (Bolte and Cordelieres, 2006) to measure 3D-object fluorescence intensity of mNG-Cdc15 assemblies along with mNG-Cdc15 total cell fluorescence.

Quantification of size and number of mNG-Cdc15 condensates

Quantitative analysis of microscopy data was performed using Fiji (a version of ImageJ software available at https://fiji.sc) (Schindelin *et al.*, 2012). All quantifications of condensate size and number were performed on deconvolved, max projected grey scale images. After splitting the channel, a threshold was fixed for the channel of interest and that threshold was made consistent through all the analyses. Max entropy with B&W settings were selected for the threshold settings. After saving the settings, the images were changed to binary mode for final final analysis of the area (size) and total number of the condensates from the selected image.

Quantification of tip septa

For Figure 5-figure supplement 2, tip septa were quantified using a previously published protocol (Bhattacharjee *et al.*, 2020). The inhibitors 3-MB-PP1 and 3-BrB-PP1 were used at a 1 μg/ml final concentrations.

Protein fluorescent labeling

Purified recombinant proteins were labelled using amine reactive NHS ester dyes (Thermo Fisher Scientific). Alexa fluorophores used to label proteins include: Cdc15 - Alexa 488 (A-20000, Thermo Fisher); Fic1 - Alexa 647 (A-20006, Thermo Fisher); Pxl1 peptide (residues 177-189) - Alexa 405 (A30000, Thermo Fisher); Cdc12 peptide

bioRxiv preprint doi: https://doi.org/10.1101/2022.08.26.505417; this version posted August 26, 2022. The copyright holder for this preprint (which was not certified by peer review) is the author/funder. All rights reserved. No reuse allowed without permission.

(residues 20-40) - Alexa 405 (A30000, Thermo Fisher). All proteins and peptide were in buffer containing 50 mM Tris, pH 7.4, 500 mM NaCl, 1 mM TCEP before addition of the fluorophores. After addition of the flurophores (fluorophores: protein molar ratio was 1:1), solutions were incubated for 1 hr on ice and excess dye was removed using Pierce Zeba Desalt Spin Columns (Thermo Scientific; 89882). Labelling efficiency of all the proteins were measured using a Nanodrop spectrophotometer (ND 1000).

In vitro LLPS assay

Phase separation of purified recombinant Cdc15-IDR-SH3 co-expressed with Pom1 was induced by treatment with λ-phosphatase (NEB; P0753L) and dilution to physiological salt concentrations (50 mM Tris pH 7.4, 150 mM NaCl final) in the presence or absence of a crowding agent (5% PEG, average molecular weight 3,350; Sigma; P4338,). Cdc15-IDR-SH3 was diluted to concentrations ranging from 5 to 50 μM and 5-10 μL was added to a glass coverslip that had been thoroughly cleaned with isopropanol and droplets were then detected by imaging. Droplets were considered to be phase separated because they showed liquid-like properties (visible rapid fusion events) and were dynamic (rapid recovery in a FRAP assay). Phase diagrams at different concentrations of salt and protein were determined within 5 minutes of phosphatase treatment.

For in vitro droplet experiments of Cdc15-IDR-SH3 with only Fic1 and Pxl1 peptide, 10 μM of each were mixed and the final salt concentration was diluted to 150 mM NaCl in the presence of 5% PEG before addition of λ-phosphatase. Images of droplets were acquired within 5 min of λ-phosphatase addition.

bioRxiv preprint doi: https://doi.org/10.1101/2022.08.26.505417; this version posted August 26, 2022. The copyright holder for this preprint (which was not certified by peer review) is the author/funder. All rights reserved. No reuse allowed without permission.

For experiments with full-length Cdc15, we used the F-BAR oligomerization mutant Cdc15-E30K, E152K prepared in 50 mM Tris pH 7.4, 500 mM NaCl, 1 mM TCEP. Cdc15, Fic1, Pxl1 peptide, and Cdc12 peptide were combined at 10 μM and diluted to a final concentration of 250 mM NaCl in the presence of 5% PEG before addition of λ-phosphatase. Images of the visible droplets were acquired by TIRF imaging within 5 min of λ-phosphatase addition.

Fluorescence recovery after photobleaching (FRAP)

FRAP analysis of the droplets were performed in a Personal DeltaVision (Cytiva Life Sciences, Marlborough, MA) that includes a microscope (IX71; Olympus), 60 × NA 1.42 Plan Apochromat and 100 × NA 1.40 U Plan S Apochromat objectives, fixed and live-cell filter wheels, a camera (a pco.edge 4.2 sCMOS), and softWoRx imaging software (Cytiva Life Sciences) as described above. Droplets with a diameter in between ~ 5-10 μm were used for FRAP measurements. A region of ~ 1-2 μm of the region of interest (partial photobleaching of the droplet) from the droplets were photobleached with a 488 laser. Images were acquired every 1s interval for 60 s and 5 images were taken prior to the photobleaching event. Quantifications of the droplets were performed using Image J. FRAP intensity measurements were corrected for background and time-course photobleaching. Each in vitro measurement for FRAP was taken from one distinct droplet and all in vitro experiments were replicated at least 3 times.

Supported lipid bilayer assay

Methods for preparing supported lipid bilayers were discussed previously (Banjade and Rosen, 2014; Day *et al.*, 2021). Lipids containing 98% DOPC (Avantilipids;850375P-

bioRxiv preprint doi: https://doi.org/10.1101/2022.08.26.505417; this version posted August 26, 2022. The copyright holder for this preprint (which was not certified by peer review) is the author/funder. All rights reserved. No reuse allowed without permission.

25mg), 2% DGS-NTA-Ni (Avantilipids;790404P-5mg) and 0.1% 18:1 PEG5000 PE (Avantilipids; 880230P-25mg) were mixed and evaporated under a nitrogen gas stream followed by drying under vacuum for 1 hr. Finally, the pellet was hydrated in a lipid buffer (25 mM HEPES, pH 7.5, 150 mM NaCl, 1 mM $MgCl_2$, 1 mM TCEP) for 30 minutes and vortexed gently before freeze-thaw. The liposome sample was passed through a filter with an extruder for 10X times to get the small unilamellar vesicles (SUVs). Prior to the experiment, coverslips and glass slides were thoroughly washed with 6 M NaOH and water followed by 70% ethanol. Clean glass slides and cover slips were then equilibrated in the previously described lipid buffer. A homemade chamber was constructed using the coverslips. Double-sided tape, glass slides, and 10-15 μL of SUVs were added into the chamber and incubated for 30 min at room temperature to allow SUVs to collapse on the glass and fuse to form the bilayer. Bilayers were washed 3 times with lipid buffer and blocked with lipid buffer containing 0.1% BSA for 30 min. After that, fluorescently-labeled His-Cdc15-IDR was added in different concentrations to the bilayer and incubated at room temperature for 1 hr. The slides were washed with lipid buffer containing 0.1% BSA to remove unbound His-tagged proteins. Fluorescently labeled His-Cdc15-IDR bound to the lipid bilayer was then visualized by TIRF microscopy.

Coarse-Grained Molecular Dynamics Simulations

Each amino acid is represented as a single bead at the location of the α carbon. Simulations were performed in either the HPS model (Dignon *et al.*, 2018; Perdikari *et al.*, 2021) or the KH model D (Kim *et al.*, 2008; Dignon *et al.*, 2018) in LAMMPS (Plimpton, 1995) using parameters described in the respective model papers unless

bioRxiv preprint doi: https://doi.org/10.1101/2022.08.26.505417; this version posted August 26, 2022. The copyright holder for this preprint (which was not certified by peer review) is the author/funder. All rights reserved. No reuse allowed without permission.

otherwise stated. In each case, pairwise interactions are modeled by Lennard-Jones-type potentials with a 3σ cutoff. We used an electrostatic screening length of 10 Å, and uniform dielectric constant 80 for electrostatic interactions of charged residues. Pairwise interactions for phosphorylated resides for the HPS model are as in (Perdikari *et al.*, 2021). For the KH model that has not been parameterized for phosphorylation, phosphorylated serine and threonine are treated as aspartic acid pair interactions, while charge and interaction radii are updated from (Perdikari *et al.*, 2021) to match the HPS model.

We represent the known structure of the F-BAR dimer [PDB 6XJ1;(Snider *et al.*, 2020)] and the Alphafold predicted structure of the Cdc15 SH3 [AF-Q09822-F1; (Jumper *et al.*, 2021) as rigid bodies using the fix rigid command in LAMMPS. All other residues of the Cdc15 sequence are represented as beads connected to their neighbors with harmonic bonds with a 3.81 Å equilibrium length and a 378 kcal/(mol $Å^2$) spring constant. For all HPS model simulations and for the KH model single chain IDR simulations, we implemented the non-bonded pairwise potential using continuous piecewise LAMMPS potentials as in (Smith *et al.*, 2021) (code available at: https://github.com/aah217/KH_LAMMPS and https://github.com/aah217/HPS_LAMMPS). We performed these simulations with the following versions of LAMMPS: “18 Apr 2015”, “21 Jul 2020”, “29 Oct 2020”, and “10 Mar 2021”. As the KH model D scales non-bonded pairwise interactions based on the solvent accessible surface area (SASA) of a residue relative to a free chain, we implemented this functionality in LAMMPS version “29 Sep 2021 - Update 1” as a custom potential utilizing code provided by Jeetain Mittal. We set the SASA-based value

bioRxiv preprint doi: https://doi.org/10.1101/2022.08.26.505417; this version posted August 26, 2022. The copyright holder for this preprint (which was not certified by peer review) is the author/funder. All rights reserved. No reuse allowed without permission.

to 1.0 for all residues not in rigid bodies (Dignon *et al.*, 2018), and as calculated at (http://curie.utmb.edu/getarea.html) (Fraczkiewicz, 1998) for residues in the F-BAR or SH3 structures. Integration was performed using a 10 fs timestep with neighbor lists updated every 10 steps. Simulations were carried out in the NVT ensemble through the use of the NVE integrator and a Langevin thermostat with a 1 ps^{-1} frictional coefficient. IDR simulations were initialized in one of two ways. For the dephosphorylated case using the HPS model, the system was started in a straight-line configuration in which the amino acids were spaced 3.81 Å apart on one axis. All other simulations were started using a semi-relaxed configuration of the IDR with an R_G of 6.53 nm. Individual trajectories were run long enough for R_G to fluctuate around an average value, with individual trajectory durations ranging from 500 ns to greater than 10 μs, with higher temperature simulations running for longer times due to computational efficiency, and between 6 and 8 trajectories for each case. For trajectories that started from a specified initial condition, as opposed to continuations, an autocorrelation function was fit to the R_G versus time data to calculate the relaxation time. Data up to twice the relaxation time were excluded from calculating the measured R_G values calculated and reported. All remaining R_G versus time data for a particular case was split into five equal parts in order to calculate the SEM.

To initialize full dimer simulations, two straight-line IDRs were placed with the amino acid next in sequence from the F-BAR dimer placed 3.81 Å from its neighbor on the F-BAR dimer with IDRs extending away from one another. Each bead in the IDR was spaced 3.81 Å apart. An SH3 domain was connected at the end of each IDR. A first pass relaxation was performed in LAMMPS for 10 ns with the spring constant reduced

bioRxiv preprint doi: https://doi.org/10.1101/2022.08.26.505417; this version posted August 26, 2022. The copyright holder for this preprint (which was not certified by peer review) is the author/funder. All rights reserved. No reuse allowed without permission.

to 0.378 kcal/(mol Å^2) and using the fix deform command to shrink the box size, and the relative spacing of its contents (excluding those fixed rigid), by a factor of ten. Follow-up simulations of 10 ns were performed to progressively increase the spring constant back to that defined by the model, making use of the nve/limit command in LAMMPs, which imposes a maximum distance that beads can travel from one timestep to the next. This method of relaxation resulted in the configuration used in the IDRs started apart simulations (Figure 6A). For the IDRs interacting initial condition (Figure 6-figure supplement 5A, B), a short simulation was performed in which a force of sufficient following from the previous steps in which strength was applied continuously to each SH3 in the direction of the opposite side of the F-BAR, causing the SH3s to cross the F-BAR dimer midplane. Follow-up simulations were performed to relax the IDRs in the new configuration using steps similar to the IDRs-apart relaxation.

Quantification and statistical analysis

Calculations of mean, standard error of the mean (SEM), and statistical significances were performed with Prism 6.0 or Prism 8.0 (GraphPad Software). Sample size (n), replicates (N), and statistical test are included in figure graph or legends. For all image analyses, no raw data were excluded with the exception of cells that were not in focus or a cell that moved during imaging.

bioRxiv preprint doi: https://doi.org/10.1101/2022.08.26.505417; this version posted August 26, 2022. The copyright holder for this preprint (which was not certified by peer review) is the author/funder. All rights reserved. No reuse allowed without permission.

Figure Legends.

Figure 1. Cdc15 is phosphorylation is regulated by polarity kinases Kin1, Shk1 and Pck1. Denatured protein lysates were prepared from the indicated strains. Anti-Cdc15 was used to immunoprecipitate (IP) Cdc15, which was then treated with λ protein phosphatase (λ) or buffer control. IP samples were separated by SDS-PAGE and immunoblotted for Cdc15 (A, C, D, E, G, H and I). (B) Denatured protein lysates from the indicated strains were separated by SDS-PAGE and then immunoblotted for Cdc15 and α-tubulin. (F) Denatured protein lysates were prepared from the indicated strains. Anti-Cdc15 was used to (IP) Cdc15 and the IPs were separated by SDS-PAGE followed by immunoblotting with anti-Cdc15 antibody.

Figure 2. Polarity kinases phosphorylate overlapping sites on Cdc15. (A-D) In vitro kinase assays were done using recombinant GST-Pom1 (A), GST-Shk1 (B), MBP-Kin1 (C) or MBP-Pck1 (D) with the indicated substrate (MBP-Cdc15C or GST-Cdc15C). After removing the first kinase, a second in vitro kinase assay was done with one of the other three kinases in the presence of radiolabeled γ-^{32}P-ATP. Kinase reactions were analyzed by SDS-PAGE, stained with Coomassie Blue (CB) (bottom) and ^{32}P incorporation was detected by autoradiography (top and middle).

bioRxiv preprint doi: https://doi.org/10.1101/2022.08.26.505417; this version posted August 26, 2022. The copyright holder for this preprint (which was not certified by peer review) is the author/funder. All rights reserved. No reuse allowed without permission.

Figure 3. Identification of Cdc15 phosphosites for Kin1, Shk1 and Pck1. (A) Schematic of Cdc15 phosphorylation mutants. Red amino acids indicate the common phosphorylation sites two or more than two kinases. (B-D) In vitro kinase assays using recombinant GST-Kin1 (B), GST-Shk1 (C) or MBP-Pck1(D) and wildtype or mutant GST-Cdc15C proteins as substrates. All kinase assays were done in the presence of radiolabeled γ-^{32}P-ATP and the reactions were separated by SDS-PAGE, stained with CB (bottom) and ^{32}P incorporation was detected by autoradiography (top). (E) Immunoprecipitation (IP) of Cdc15 of the indicated strain, which was then treated with λ protein phosphatase (λ) or buffer control. (F) Cell lysates prepared from the indicated genotypes and arrests were subjected to IP for Cdc15. For E and F, samples were separated by SDS-PAGE and immunoblotted for Cdc15.

Figure 4. Quantification of mNG-Cdc15 abundance in the CR and cytokinesis dynamics of Cdc15 phosphomutants. (A ,C) Quantification of the fluorescence intensities of Cdc15 (A) and Rlc1 (C) in the fully formed CR and constricted CR of wildtype and *cdc15-31A* cells. N≥ 29 cells from 3 biological replicates. Error bars indicate SEM. (B) Quantification of the whole cell fluorescence intensity of *mNG-cdc15* and *mNG-cdc15-31A* cells. N≥ 26 cells from 3 biological replicates. Error bars indicate SEM. (D) Representative montages from live cell time lapse images of the indicated strains. Images were acquired every 2 min and every 4 min are shown. Numbers indicate min from SPB separation. Scale bar, 2 μm. (E) Quantification of the length of cytokinesis of the indicated strains from 3 biological replicates. N≥ 21 cells. Error bars indicate SEM. All statistical comparisons were made using non-parametric T-test with

bioRxiv preprint doi: https://doi.org/10.1101/2022.08.26.505417; this version posted August 26, 2022. The copyright holder for this preprint (which was not certified by peer review) is the author/funder. All rights reserved. No reuse allowed without permission.

Mann Whitney test. *p<0.05, **p< 0.01, ***p<0.001 and ****p< 0.0001. ns= non-significant.

Figure 5. Quantification of mNG-Cdc15 localization ratio of membrane to cytoplasm in kinase and Cdc15 phospho-mutants. (A) Quantification of membrane to cytoplasm ratio of mNG-Cdc15 (a.u.) of the indicated strains after treatment with inhibitor(s) 15 μM 3-MB-PP1 and/or 30 μM 3BrB-PP1 for 15 minutes. n≥ 97 cells (B, C) Quantification of membrane to cytoplasm ratio of mNG-Cdc15 (A.U) of the indicated strains. n≥ 65 (B) and n≥ 97 cells (C) respectively. Error bars indicate SEM. Comparisons were made from 3 independent experiments using one-way ANOVA with Tukey's multiple comparison test. ****p< 0.0001 and ns= non-significant, p>0.05.

Figure 6. Coarse-grained molecular dynamics of Cdc15 using the HPS model show large conformational transition induced by phosphorylation of its IDR region. (A) Snapshot of an α-carbon representation of a Cdc15 dimer with each amino acid represented by a single bead. The F-BAR and SH3 regions are kept rigid (PDB: 6XJ1 and AlphaFold model AF-Q09822-F1, respectively). All other residues connected with flexible linkers (inset). Snapshot shows the initial condition with the IDRs started apart from each other. (B) Representative simulation snapshots of the indicated phosphorylation state: Deph has no phosphorylation, Full includes all sites from Figure 3, otherwise the label states that the model includes all sites of the named kinase. (C) Frequency distribution of distance between the center of mass (COM) of each IDR. Grey line indicates 100 Å. Ten independent simulations of at least 1.9 μs were performed for each phosphorylation state with half initialized with the IDRs apart (panel A or Figure 6-figure supplement 5A) and half with the IDRs

bioRxiv preprint doi: https://doi.org/10.1101/2022.08.26.505417; this version posted August 26, 2022. The copyright holder for this preprint (which was not certified by peer review) is the author/funder. All rights reserved. No reuse allowed without permission.

interacting (Figure 6- figure supplement 5B). (D) Fraction of trajectories of indicated states with COM separation greater than 100 Å. (E) Representative snapshots of simulations of single Cdc15 IDR (residues 327-854, connected with flexible linkers) in different phosphorylation states. (F) Average radius of gyration, R_G, versus net charge of the chain (phosphorylation charge treated as -2e.) Error bars indicate SEM.

Figure 7. The dynamic properties of dephosphorylated Cdc15 condensates.

(A) Phase diagrams showing whether purified Cdc15-IDR-SH3 labeled with Alexa-488 succinimide ester dye forms condensates at different protein concentrations, NaCl concentrations, and phosphatase treatment. (B) In vitro droplet formation at different concentrations of Cdc15-IDR-SH3 in 50 mM Tris pH 7.4, 150 mM NaCl with 5% PEG after treatment with λ (lower panel). Scale bar, 10 μm. (C) Time-lapse analysis showing fusion of droplets containing Cdc15-IDR-SH3 after treatment with λ. Phase separation assays were performed in 50 mM Tris pH 7.4, 150 mM NaCl. Scale bar, 5 μm. (D) Quantified FRAP dynamics of Cdc15–IDR-SH3 condensates after partial bleaching. In this experiment, condensates were formed in 50 mM Tris pH 7.4, 150 mM NaCl without PEG and with 25 μM of protein. N=10 from 3 independent experiments. (E) Fluorescent image (top) and line scan (bottom) performed through the center of each droplet. (F) Incorporation index (I_{inc}= $Intensity_{center}$ / $Intensity_{edge}$) for Cdc15-IDR- Alexa-488 when dephosphorylated at 50 mM Tris pH 7.4, 150 mM NaCl, 5% PEG with 25 μM of protein. (G and H) TIRF imaging was used to detect condensates of labeled Cdc15-IDR-SH3 on supported lipid bilayers. (G) Phase diagrams for purified Cdc15-IDR-SH3 labeled with Alexa-488 on a supported lipid bilayer, showing protein concentrations versus NaCl

bioRxiv preprint doi: https://doi.org/10.1101/2022.08.26.505417; this version posted August 26, 2022. The copyright holder for this preprint (which was not certified by peer review) is the author/funder. All rights reserved. No reuse allowed without permission.

concentrations. (H) In vitro droplet formation at 25 μM Cdc15-IDR-SH3 on a supported lipid bilayer after treatment with λ in 50 mM Tris pH 7.4, 250 mM NaCl. Scale bar, 5 μm.

Figure 8. Cdc15 promotes in vitro phase separation along with its F-BAR and SH3 domain binding partners, Fic1, Pxl1 and Cdc12. (A) Fluorescence images of the droplets formed from in vitro assays when Cdc15-IDR-SH3 (Alexa 488 labeled), Fic1 (Alexa 647 labeled) and Pxl1 (residues 177-188; Alexa 405 labeled) were mixed at 10 μM concentration each and then dephosphorylated with λ phosphatase. Phase separation assays were performed in 50 mM Tris pH 7.4, 150 mM NaCl, and 5% PEG. (B) Fluorescence images of the droplets formed with: TOP- 10 μM each full length Cdc15 (E30K, E152K) (Alexa 488 labeled), treated with λ phosphatase and incubated with Fic1 (Alexa 647 labeled), Pxl1 (residues 177-188; Alexa 405 labeled), and Cdc12 (residues 20-40; unlabeled). BOTTOM- 10 μM each of full length Cdc15 (E30K, E152K) (Alexa 488 labeled) treated with λ phosphatase and incubated with Fic1 (Alexa 647 labeled), Pxl1 (residues 177-188; unlabeled) and Cdc12 (residues 20-40; Alexa 405 labeled). Phase separation assays were performed in 50 mM Tris pH 7.4, 250 mM NaCl with 5% PEG. Scale bars, 5 μm.

Figure 9. Cdc15 assembles into condensates and shows dynamic property in vivo. (A, B) Quantification of the number (A) and size (B) of Cdc15 condensates in the cortex of the indicated strains during interphase. N≥ 10 cells. Error bars indicate SEM. Comparisons were made from 3 independent experiments using one-way ANOVA with Tukey's multiple comparison test. *p<0.05, **p< 0.01, ***p< 0.001 and ****p< 0.0001. (C) mNG-Cdc15 condensates undergoing apparent fission (top) and fusion (bottom) events in *mNG-cdc15-31A* strain. Scale bar, 2 μm. (D) Representative images to show

bioRxiv preprint doi: https://doi.org/10.1101/2022.08.26.505417; this version posted August 26, 2022. The copyright holder for this preprint (which was not certified by peer review) is the author/funder. All rights reserved. No reuse allowed without permission.

Fic1-mNG (left), Rlc1-mNG (right) co-localizing with Cdc15-mCherry from the indicated *cdc15-wt* and *cdc15-31A* strains. Scale bar, 5 μm.

Videos.

Video 1. Simulation of Cdc15 dimer in the HPS model with IDRs started apart. The Cdc15 dimer is represented as described in Figure 6A. One of the five independent trajectories is shown starting in the IDRs apart initial condition (Figure 6-figure supplement 1A) for both the dephosphorylated case (top) and the fully phosphorylated case (bottom). In the dephosphorylated case the IDRs from each chain spend the majority of the time interacting with each other near the center of the F-BAR. For the fully phosphorylated case the IDRs mostly remain separated and localized to the F-BAR poles while occasionally interacting with each other.

Video 2. Simulation of Cdc15 dimer in the HPS model with IDRs started interacting. Same as Video 1 but starting in the IDRs interacting initial condition (Figure 6-figure supplement 1B). In the dephosphorylated case the IDRs from each chain remain interacting with each other and localize mostly towards the center of the F-BAR. In the fully phosphorylated case the IDRs are able to separate from each other (1776 ns) and are localized less to the center of the F-BAR throughout the trajectory.

Video 3. Fusion event of Cdc15-IDR-SH3 droplet represented at Figure 7C.

Video 4 and 5. Apparent fission (Video 4) and fusion (Video 5) events of the mNG-Cdc15 condensates in mNG-Cdc15-31A strain shown in Figure 9C.

bioRxiv preprint doi: https://doi.org/10.1101/2022.08.26.505417; this version posted August 26, 2022. The copyright holder for this preprint (which was not certified by peer review) is the author/funder. All rights reserved. No reuse allowed without permission.

References

Akamatsu, M., Berro, J., Pu, K.M., Tebbs, I.R., and Pollard, T.D. (2014). Cytokinetic nodes in fission yeast arise from two distinct types of nodes that merge during interphase. J Cell Biol *204*, 977-988.

Arasada, R., and Pollard, T.D. (2011). Distinct roles for F-BAR proteins Cdc15p and Bzz1p in actin polymerization at sites of endocytosis in fission yeast. Curr Biol *21*, 1450-1459.

Arellano, M., Coll, P.M., and Perez, P. (1999). RHO GTPases in the control of cell morphology, cell polarity, and actin localization in fission yeast. Microsc Res Tech *47*, 51-60.

Bahler, J., Steever, A.B., Wheatley, S., Wang, Y., Pringle, J.R., Gould, K.L., and McCollum, D. (1998). Role of polo kinase and Mid1p in determining the site of cell division in fission yeast. J Cell Biol *143*, 1603-1616.

Balasubramanian, M.K., Bi, E., and Glotzer, M. (2004). Comparative analysis of cytokinesis in budding yeast, fission yeast and animal cells. Curr Biol *14*, R806-818.

Banjade, S., and Rosen, M.K. (2014). Phase transitions of multivalent proteins can promote clustering of membrane receptors. Elife *3*.

Bhatia, P., Hachet, O., Hersch, M., Rincon, S.A., Berthelot-Grosjean, M., Dalessi, S., Basterra, L., Bergmann, S., Paoletti, A., and Martin, S.G. (2014). Distinct levels in Pom1 gradients limit Cdr2 activity and localization to time and position division. Cell Cycle *13*, 538-552.

Bhattacharjee, R., Mangione, M.C., Wos, M., Chen, J.S., Snider, C.E., Roberts-Galbraith, R.H., McDonald, N.A., Presti, L.L., Martin, S.G., and Gould, K.L. (2020). DYRK kinase Pom1 drives F-BAR protein Cdc15 from the membrane to promote medial division. Mol Biol Cell *31*, 917-929.

Bienkiewicz, E.A., and Lumb, K.J. (1999). Random-coil chemical shifts of phosphorylated amino acids. J Biomol NMR *15*, 203-206.

Bohnert, K.A., Rossi, A.M., Jin, Q.W., Chen, J.S., and Gould, K.L. (2020). Phosphoregulation of the Cytokinetic Protein Fic1 Contributes to Fission Yeast Growth Polarity Establishment. J Cell Sci.

Bolte, S., and Cordelieres, F.P. (2006). A guided tour into subcellular colocalization analysis in light microscopy. J Microsc *224*, 213-232.

Boyle, W.J., van der Geer, P., and Hunter, T. (1991). Phosphopeptide mapping and phosphoamino acid analysis by two-dimensional separation on thin-layer cellulose plates. Methods Enzymol *201*, 110-149.

Cadou, A., Couturier, A., Le Goff, C., Soto, T., Miklos, I., Sipiczki, M., Xie, L., Paulson, J.R., Cansado, J., and Le Goff, X. (2010). Kin1 is a plasma membrane-associated kinase that regulates the cell surface in fission yeast. Mol Microbiol *77*, 1186-1202.

Calvert, M.E., Wright, G.D., Leong, F.Y., Chiam, K.H., Chen, Y., Jedd, G., and Balasubramanian, M.K. (2011). Myosin concentration underlies cell size-dependent scalability of actomyosin ring constriction. J Cell Biol *195*, 799-813.

Carnahan, R.H., and Gould, K.L. (2003). The PCH family protein, Cdc15p, recruits two F-actin nucleation pathways to coordinate cytokinetic actin ring formation in Schizosaccharomyces pombe. J Cell Biol *162*, 851-862.

Case, L.B., De Pasquale, M., Henry, L., and Rosen, M.K. (2022). Synergistic phase separation of two pathways promotes integrin clustering and nascent adhesion formation. Elife *11*.

Celton-Morizur, S., Racine, V., Sibarita, J.B., and Paoletti, A. (2006). Pom1 kinase links division plane position to cell polarity by regulating Mid1p cortical distribution. J Cell Sci *119*, 4710-4718.

Chang, F., Woollard, A., and Nurse, P. (1996). Isolation and characterization of fission yeast mutants defective in the assembly and placement of the contractile actin ring. J Cell Sci *109 (Pt 1)*, 131-142.

bioRxiv preprint doi: https://doi.org/10.1101/2022.08.26.505417; this version posted August 26, 2022. The copyright holder for this preprint (which was not certified by peer review) is the author/funder. All rights reserved. No reuse allowed without permission.

Chatterjee, M., and Pollard, T.D. (2019). The Functionally Important N-Terminal Half of Fission Yeast Mid1p Anillin Is Intrinsically Disordered and Undergoes Phase Separation. Biochemistry *58*, 3031-3041.
Chen, D., Cao, X., Tao, Y., Wu, Q., Pan, Y., Peng, D., Liu, Z., Huang, L., Wang, Y., Wang, X., and Yuan, Z. (2013). Development of a liquid chromatography-tandem mass spectrometry with ultrasound-assisted extraction and auto solid-phase clean-up method for the determination of Fusarium toxins in animal derived foods. J Chromatogr A *1311*, 21-29.
Cipak, L., Zhang, C., Kovacikova, I., Rumpf, C., Miadokova, E., Shokat, K.M., and Gregan, J. (2011). Generation of a set of conditional analog-sensitive alleles of essential protein kinases in the fission yeast Schizosaccharomyces pombe. Cell Cycle *10*, 3527-3532.
Clifford, D.M., Wolfe, B.A., Roberts-Galbraith, R.H., McDonald, W.H., Yates, J.R., 3rd, and Gould, K.L. (2008). The Clp1/Cdc14 phosphatase contributes to the robustness of cytokinesis by association with anillin-related Mid1. J Cell Biol *181*, 79-88.
Coffman, V.C., Nile, A.H., Lee, I.J., Liu, H., and Wu, J.Q. (2009). Roles of formin nodes and myosin motor activity in Mid1p-dependent contractile-ring assembly during fission yeast cytokinesis. Mol Biol Cell *20*, 5195-5210.
Cortes, J.C., Pujol, N., Sato, M., Pinar, M., Ramos, M., Moreno, B., Osumi, M., Ribas, J.C., and Perez, P. (2015). Cooperation between Paxillin-like Protein Pxl1 and Glucan Synthase Bgs1 Is Essential for Actomyosin Ring Stability and Septum Formation in Fission Yeast. PLoS Genet *11*, e1005358.
Das, R.K., and Pappu, R.V. (2013). Conformations of intrinsically disordered proteins are influenced by linear sequence distributions of oppositely charged residues. Proc Natl Acad Sci U S A *110*, 13392-13397.
Day, K.J., Kago, G., Wang, L., Richter, J.B., Hayden, C.C., Lafer, E.M., and Stachowiak, J.C. (2021). Liquid-like protein interactions catalyse assembly of endocytic vesicles. Nat Cell Biol *23*, 366-376.
Dephoure, N., Gould, K.L., Gygi, S.P., and Kellogg, D.R. (2013). Mapping and analysis of phosphorylation sites: a quick guide for cell biologists. Mol Biol Cell *24*, 535-542.
Dignon, G.L., Zheng, W., Kim, Y.C., Best, R.B., and Mittal, J. (2018). Sequence determinants of protein phase behavior from a coarse-grained model. PLoS Comput Biol *14*, e1005941.
Fankhauser, C., Reymond, A., Cerutti, L., Utzig, S., Hofmann, K., and Simanis, V. (1995). The *S. pombe cdc15* gene is a key element in the reorganization of F- actin at mitosis [published erratum appears in Cell 1997 Jun 27;89(7):1185]. Cell *82*, 435-444.
Fraczkiewicz, R. (1998). Exact and efficient analytical calculation of the accessible surface areas and their gradients for macromolecules. Journal of Computational Chemistry *19*, 319-333.
Gietz, R.D., Schiestl, R.H., Willems, A.R., and Woods, R.A. (1995). Studies on the transformation of intact yeast cells by the LiAc/SS-DNA/PEG procedure. Yeast *11*, 355-360.
Hachet, O., Berthelot-Grosjean, M., Kokkoris, K., Vincenzetti, V., Moosbrugger, J., and Martin, S.G. (2011). A phosphorylation cycle shapes gradients of the DYRK family kinase Pom1 at the plasma membrane. Cell *145*, 1116-1128.
Hachet, O., and Simanis, V. (2008). Mid1p/anillin and the septation initiation network orchestrate contractile ring assembly for cytokinesis. Genes Dev *22*, 3205-3216.
Harris, M.A., Rutherford, K.M., Hayles, J., Lock, A., Bahler, J., Oliver, S.G., Mata, J., and Wood, V. (2022). Fission stories: using PomBase to understand Schizosaccharomyces pombe biology. Genetics *220*.
Huang, Y., Chew, T.G., Ge, W., and Balasubramanian, M.K. (2007). Polarity determinants Tea1p, Tea4p, and Pom1p inhibit division-septum assembly at cell ends in fission yeast. Developmental cell *12*, 987-996.
Jacobs, W.M., and Frenkel, D. (2017). Phase Transitions in Biological Systems with Many Components. Biophys J *112*, 683-691.

bioRxiv preprint doi: https://doi.org/10.1101/2022.08.26.505417; this version posted August 26, 2022. The copyright holder for this preprint (which was not certified by peer review) is the author/funder. All rights reserved. No reuse allowed without permission.

Jumper, J., Evans, R., Pritzel, A., Green, T., Figurnov, M., Ronneberger, O., Tunyasuvunakool, K., Bates, R., Zidek, A., Potapenko, A., Bridgland, A., Meyer, C., Kohl, S.A.A., Ballard, A.J., Cowie, A., Romera-Paredes, B., Nikolov, S., Jain, R., Adler, J., Back, T., Petersen, S., Reiman, D., Clancy, E., Zielinski, M., Steinegger, M., Pacholska, M., Berghammer, T., Bodenstein, S., Silver, D., Vinyals, O., Senior, A.W., Kavukcuoglu, K., Kohli, P., and Hassabis, D. (2021). Highly accurate protein structure prediction with AlphaFold. Nature *596*, 583-589.

Kamnev, A., Palani, S., Zambon, P., Cheffings, T., Burroughs, N., and Balasubramanian, M.K. (2021). Time-varying mobility and turnover of actomyosin ring components during cytokinesis in Schizosaccharomyces pombe. Mol Biol Cell *32*, 237-246.

Kapcha, L.H., and Rossky, P.J. (2014). A simple atomic-level hydrophobicity scale reveals protein interfacial structure. J Mol Biol *426*, 484-498.

Keeney, J.B., and Boeke, J.D. (1994). Efficient targeted integration at leu1-32 and ura4-294 in Schizosaccharomyces pombe. Genetics *136*, 849-856.

Kettenbach, A.N., Deng, L., Wu, Y., Baldissard, S., Adamo, M.E., Gerber, S.A., and Moseley, J.B. (2015). Quantitative phosphoproteomics reveals pathways for coordination of cell growth and division by the conserved fission yeast kinase pom1. Mol Cell Proteomics *14*, 1275-1287.

Kim, Y.C., Tang, C., Clore, G.M., and Hummer, G. (2008). Replica exchange simulations of transient encounter complexes in protein-protein association. Proc Natl Acad Sci U S A *105*, 12855-12860.

Kobori, H., Toda, T., Yaguchi, H., Toya, M., Yanagida, M., and Osumi, M. (1994). Fission yeast protein kinase C gene homologues are required for protoplast regeneration: a functional link between cell wall formation and cell shape control. J Cell Sci *107 (Pt 5)*, 1131-1136.

Kozak, M., and Kaksonen, M. (2022). Condensation of Ede1 promotes the initiation of endocytosis. Elife *11*.

Laplante, C., Huang, F., Tebbs, I.R., Bewersdorf, J., and Pollard, T.D. (2016). Molecular organization of cytokinesis nodes and contractile rings by super-resolution fluorescence microscopy of live fission yeast. Proc Natl Acad Sci U S A *113*, E5876-E5885.

Laporte, D., Coffman, V.C., Lee, I.J., and Wu, J.Q. (2011). Assembly and architecture of precursor nodes during fission yeast cytokinesis. J Cell Biol *192*, 1005-1021.

Lee, M.E., Rusin, S.F., Jenkins, N., Kettenbach, A.N., and Moseley, J.B. (2018). Mechanisms Connecting the Conserved Protein Kinases Ssp1, Kin1, and Pom1 in Fission Yeast Cell Polarity and Division. Curr Biol *28*, 84-92 e84.

Lin, Y.H., and Chan, H.S. (2017). Phase Separation and Single-Chain Compactness of Charged Disordered Proteins Are Strongly Correlated. Biophys J *112*, 2043-2046.

Magliozzi, J.O., Sears, J., Cressey, L., Brady, M., Opalko, H.E., Kettenbach, A.N., and Moseley, J.B. (2020). Fission yeast Pak1 phosphorylates anillin-like Mid1 for spatial control of cytokinesis. J Cell Biol *219*.

Mangione, M.C., Snider, C.E., and Gould, K.L. (2019). The intrinsically disordered region of the cytokinetic F-BAR protein Cdc15 performs a unique essential function in maintenance of cytokinetic ring integrity. Mol Biol Cell *30*, 2790-2801.

Martin, S.G., and Berthelot-Grosjean, M. (2009). Polar gradients of the DYRK-family kinase Pom1 couple cell length with the cell cycle. Nature *459*, 852-856.

Martin-Garcia, R., Arribas, V., Coll, P.M., Pinar, M., Viana, R.A., Rincon, S.A., Correa-Bordes, J., Ribas, J.C., and Perez, P. (2018). Paxillin-Mediated Recruitment of Calcineurin to the Contractile Ring Is Required for the Correct Progression of Cytokinesis in Fission Yeast. Cell Rep *25*, 772-783 e774.

McDonald, N.A., Lind, A.L., Smith, S.E., Li, R., and Gould, K.L. (2017). Nanoscale architecture of the Schizosaccharomyces pombe contractile ring. Elife *6*.

McDonald, N.A., Vander Kooi, C.W., Ohi, M.D., and Gould, K.L. (2015). Oligomerization but Not Membrane Bending Underlies the Function of Certain F-BAR Proteins in Cell Motility and Cytokinesis. Developmental cell *35*, 725-736.

bioRxiv preprint doi: https://doi.org/10.1101/2022.08.26.505417; this version posted August 26, 2022. The copyright holder for this preprint (which was not certified by peer review) is the author/funder. All rights reserved. No reuse allowed without permission.

Miyazawa, S., and Jernigan, R.L. (1996). Residue-residue potentials with a favorable contact pair term and an unfavorable high packing density term, for simulation and threading. J Mol Biol *256*, 623-644.
Monahan, Z., Ryan, V.H., Janke, A.M., Burke, K.A., Rhoads, S.N., Zerze, G.H., O'Meally, R., Dignon, G.L., Conicella, A.E., Zheng, W., Best, R.B., Cole, R.N., Mittal, J., Shewmaker, F., and Fawzi, N.L. (2017). Phosphorylation of the FUS low-complexity domain disrupts phase separation, aggregation, and toxicity. EMBO J *36*, 2951-2967.
Moreno, S., Klar, A., and Nurse, P. (1991). Molecular genetic analysis of fission yeast Schizosaccharomyces pombe. Methods Enzymol *194*, 795-823.
Nurse, P., Thuriaux, P., and Nasmyth, K. (1976). Genetic control of the cell division cycle in the fission yeast Schizosaccharomyces pombe. Mol Gen Genet *146*, 167-178.
Padte, N.N., Martin, S.G., Howard, M., and Chang, F. (2006). The cell-end factor pom1p inhibits mid1p in specification of the cell division plane in fission yeast. Curr Biol *16*, 2480-2487.
Paoletti, A., and Chang, F. (2000). Analysis of mid1p, a protein required for placement of the cell division site, reveals a link between the nucleus and the cell surface in fission yeast. Mol Biol Cell *11*, 2757-2773.
Perdikari, T.M., Jovic, N., Dignon, G.L., Kim, Y.C., Fawzi, N.L., and Mittal, J. (2021). A predictive coarse-grained model for position-specific effects of post-translational modifications. Biophys J *120*, 1187-1197.
Plimpton, S. (1995). Fast Parallel Algorithms for Short-Range Molecular Dynamic. Journal of Computational Physics *117*, 1-19.
Pollard, T.D., and O'Shaughnessy, B. (2019). Molecular Mechanism of Cytokinesis. Annu Rev Biochem *88*, 661-689.
Pollard, T.D., and Wu, J.Q. (2010). Understanding cytokinesis: lessons from fission yeast. Nat Rev Mol Cell Biol *11*, 149-155.
Ren, L., Willet, A.H., Roberts-Galbraith, R.H., McDonald, N.A., Feoktistova, A., Chen, J.S., Huang, H., Guillen, R., Boone, C., Sidhu, S.S., Beckley, J.R., and Gould, K.L. (2015). The Cdc15 and Imp2 SH3 domains cooperatively scaffold a network of proteins that redundantly ensure efficient cell division in fission yeast. Molecular biology of the cell *26*, 256-269.
Rincon, S.A., and Paoletti, A. (2012). Mid1/anillin and the spatial regulation of cytokinesis in fission yeast. Cytoskeleton (Hoboken) *69*, 764-777.
Rincon, S.A., and Paoletti, A. (2016). Molecular control of fission yeast cytokinesis. Semin Cell Dev Biol *53*, 28-38.
Roberts-Galbraith, R.H., Chen, J.S., Wang, J., and Gould, K.L. (2009). The SH3 domains of two PCH family members cooperate in assembly of the Schizosaccharomyces pombe contractile ring. J Cell Biol *184*, 113-127.
Roberts-Galbraith, R.H., and Gould, K.L. (2010). Setting the F-BAR: functions and regulation of the F-BAR protein family. Cell Cycle *9*, 4091-4097.
Roberts-Galbraith, R.H., Ohi, M.D., Ballif, B.A., Chen, J.S., McLeod, I., McDonald, W.H., Gygi, S.P., Yates, J.R., 3rd, and Gould, K.L. (2010). Dephosphorylation of F-BAR protein Cdc15 modulates its conformation and stimulates its scaffolding activity at the cell division site. Mol Cell *39*, 86-99.
Sanchez-Mir, L., Soto, T., Franco, A., Madrid, M., Viana, R.A., Vicente, J., Gacto, M., Perez, P., and Cansado, J. (2014). Rho1 GTPase and PKC ortholog Pck1 are upstream activators of the cell integrity MAPK pathway in fission yeast. PLoS One *9*, e88020.
Schindelin, J., Arganda-Carreras, I., Frise, E., Kaynig, V., Longair, M., Pietzsch, T., Preibisch, S., Rueden, C., Saalfeld, S., Schmid, B., Tinevez, J.Y., White, D.J., Hartenstein, V., Eliceiri, K., Tomancak, P., and Cardona, A. (2012). Fiji: an open-source platform for biological-image analysis. Nat Methods *9*, 676-682.
Shea, J.E., Best, R.B., and Mittal, J. (2021). Physics-based computational and theoretical approaches to intrinsically disordered proteins. Curr Opin Struct Biol *67*, 219-225.

bioRxiv preprint doi: https://doi.org/10.1101/2022.08.26.505417; this version posted August 26, 2022. The copyright holder for this preprint (which was not certified by peer review) is the author/funder. All rights reserved. No reuse allowed without permission.

Smith, H., Pinkerton, N., Heisler, D.B., Kudryashova, E., Hall, A.R., Karch, K.R., Norris, A., Wysocki, V., Sotomayor, M., Reisler, E., Vavylonis, D., and Kudryashov, D.S. (2021). Rounding Out the Understanding of ACD Toxicity with the Discovery of Cyclic Forms of Actin Oligomers. Int J Mol Sci *22*.

Snider, C.E., Bhattacharjee, R., Igarashi, M.G., and Gould, K.L. (2022). Fission yeast paxillin contains two Cdc15 binding motifs for robust recruitment to the cytokinetic ring. Mol Biol Cell *33*, br4.

Snider, C.E., Chandra, M., McDonald, N.A., Willet, A.H., Collier, S.E., Ohi, M.D., Jackson, L.P., and Gould, K.L. (2020). Opposite Surfaces of the Cdc15 F-BAR Domain Create a Membrane Platform That Coordinates Cytoskeletal and Signaling Components for Cytokinesis. Cell Rep *33*, 108526.

Sohrmann, M., Fankhauser, C., Brodbeck, C., and Simanis, V. (1996). The dmf1/mid1 gene is essential for correct positioning of the division septum in fission yeast. Genes Dev *10*, 2707-2719.

Swaffer, M.P., Jones, A.W., Flynn, H.R., Snijders, A.P., and Nurse, P. (2018). Quantitative Phosphoproteomics Reveals the Signaling Dynamics of Cell-Cycle Kinases in the Fission Yeast Schizosaccharomyces pombe. Cell Rep *24*, 503-514.

Toda, T., Shimanuki, M., and Yanagida, M. (1993). Two novel protein kinase C-related genes of fission yeast are essential for cell viability and implicated in cell shape control. EMBO J *12*, 1987-1995.

Varadi, M., Anyango, S., Deshpande, M., Nair, S., Natassia, C., Yordanova, G., Yuan, D., Stroe, O., Wood, G., Laydon, A., Zidek, A., Green, T., Tunyasuvunakool, K., Petersen, S., Jumper, J., Clancy, E., Green, R., Vora, A., Lutfi, M., Figurnov, M., Cowie, A., Hobbs, N., Kohli, P., Kleywegt, G., Birney, E., Hassabis, D., and Velankar, S. (2022). AlphaFold Protein Structure Database: massively expanding the structural coverage of protein-sequence space with high-accuracy models. Nucleic Acids Res *50*, D439-D444.

Verde, F., Mata, J., and Nurse, P. (1995). Fission yeast cell morphogenesis: identification of new genes and analysis of their role during the cell cycle. J Cell Biol *131*, 1529-1538.

Waters, J.C. (2009). Accuracy and precision in quantitative fluorescence microscopy. J Cell Biol *185*, 1135-1148.

Willet, A.H., DeWitt, A.K., Beckley, J.R., Clifford, D.M., and Gould, K.L. (2019). NDR Kinase Sid2 Drives Anillin-like Mid1 from the Membrane to Promote Cytokinesis and Medial Division Site Placement. Curr Biol *29*, 1055-1063 e1052.

Willet, A.H., McDonald, N.A., Bohnert, K.A., Baird, M.A., Allen, J.R., Davidson, M.W., and Gould, K.L. (2015a). The F-BAR Cdc15 promotes contractile ring formation through the direct recruitment of the formin Cdc12. The Journal of cell biology *208*, 391-399.

Willet, A.H., McDonald, N.A., and Gould, K.L. (2015b). Regulation of contractile ring formation and septation in Schizosaccharomyces pombe. Curr Opin Microbiol *28*, 46-52.

Wu, J.Q., Kuhn, J.R., Kovar, D.R., and Pollard, T.D. (2003). Spatial and temporal pathway for assembly and constriction of the contractile ring in fission yeast cytokinesis. Dev Cell *5*, 723-734.

Wu, J.Q., and Pollard, T.D. (2005). Counting cytokinesis proteins globally and locally in fission yeast. Science *310*, 310-314.

Wu, J.Q., Sirotkin, V., Kovar, D.R., Lord, M., Beltzner, C.C., Kuhn, J.R., and Pollard, T.D. (2006). Assembly of the cytokinetic contractile ring from a broad band of nodes in fission yeast. J Cell Biol *174*, 391-402.

bioRxiv preprint doi: https://doi.org/10.1101/2022.08.26.505417; this version posted August 26, 2022. The copyright holder for this preprint (which was not certified by peer review) is the author/funder. All rights reserved. No reuse allowed without permission.

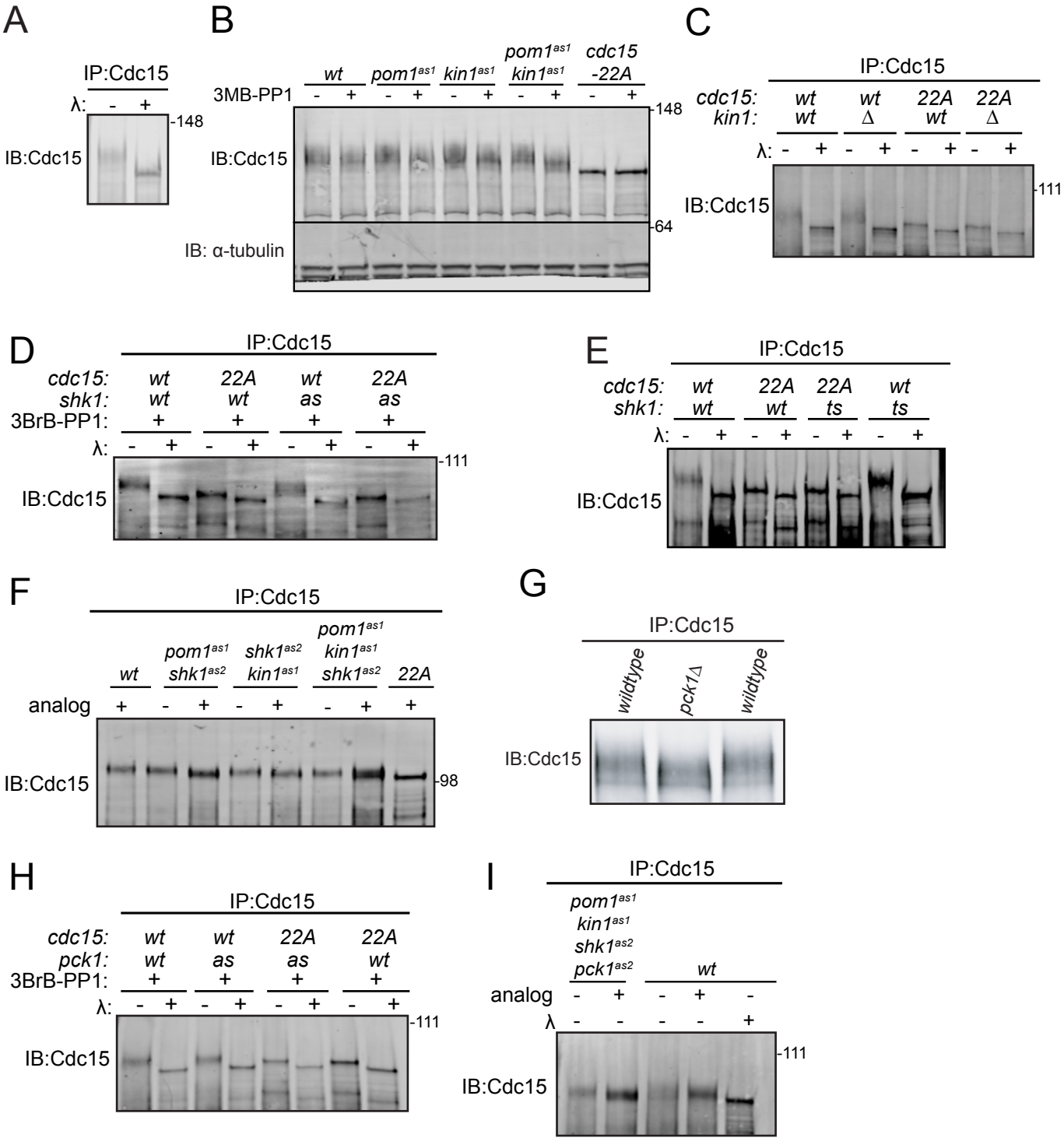

Figure 1

bioRxiv preprint doi: https://doi.org/10.1101/2022.08.26.505417; this version posted August 26, 2022. The copyright holder for this preprint (which was not certified by peer review) is the author/funder. All rights reserved. No reuse allowed without permission.

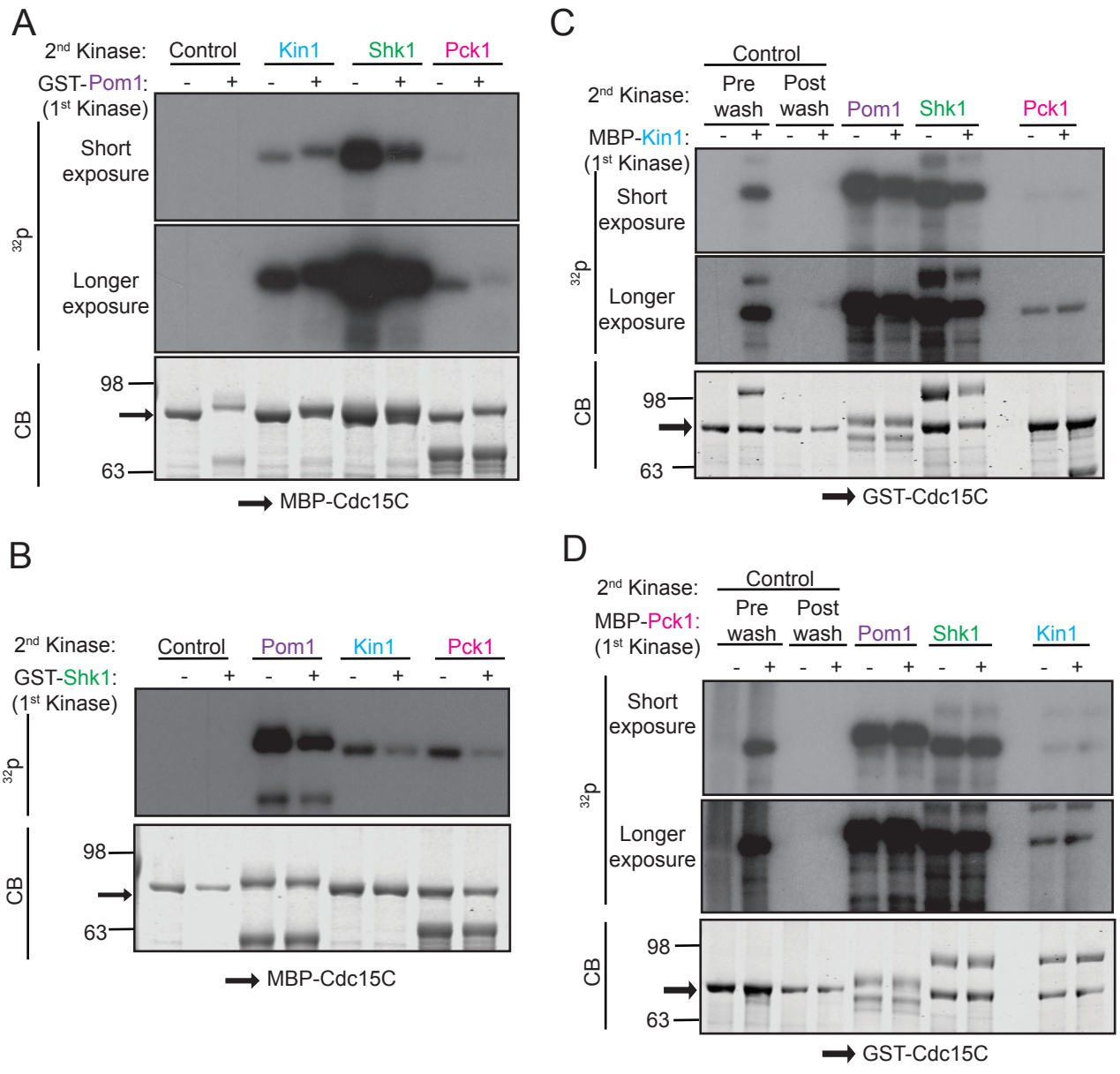

Figure 2

bioRxiv preprint doi: https://doi.org/10.1101/2022.08.26.505417; this version posted August 26, 2022. The copyright holder for this preprint (which was not certified by peer review) is the author/funder. All rights reserved. No reuse allowed without permission.

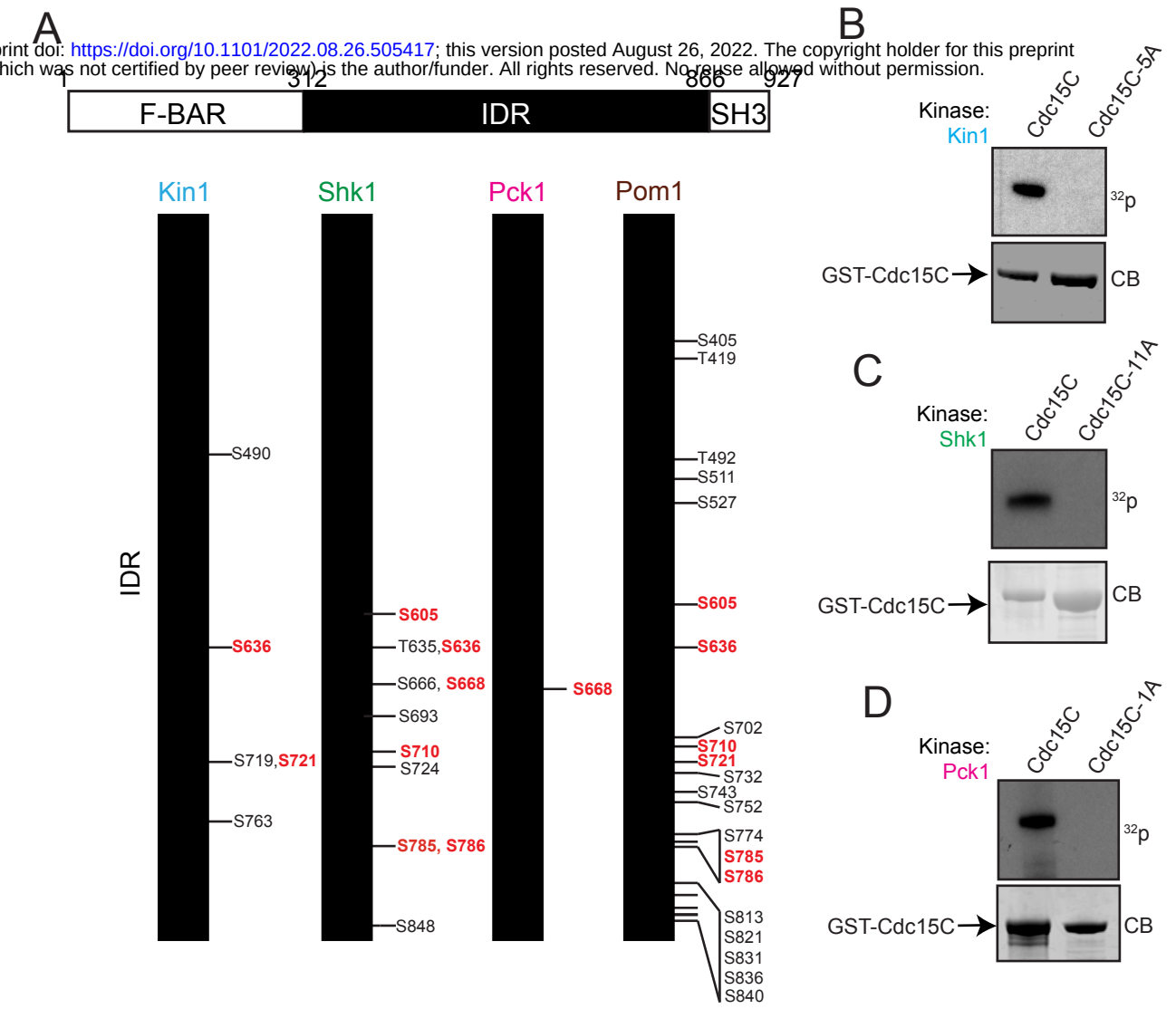

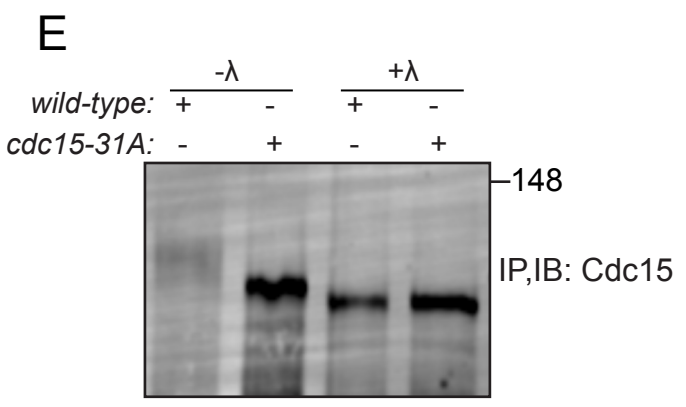

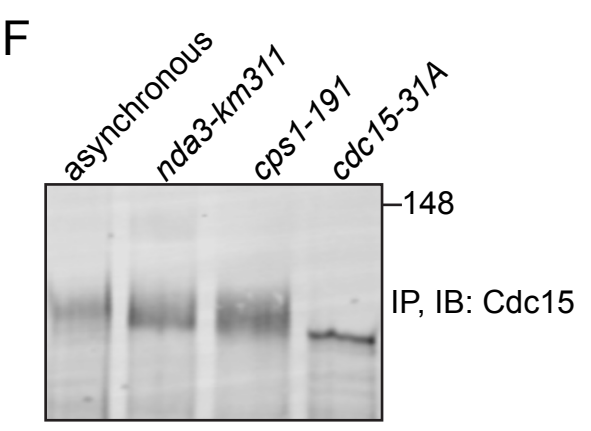

Figure 3

bioRxiv preprint doi: https://doi.org/10.1101/2022.08.26.505417; this version posted August 26, 2022. The copyright holder for this preprint (which was not certified by peer review) is the author/funder. All rights reserved. No reuse allowed without permission.

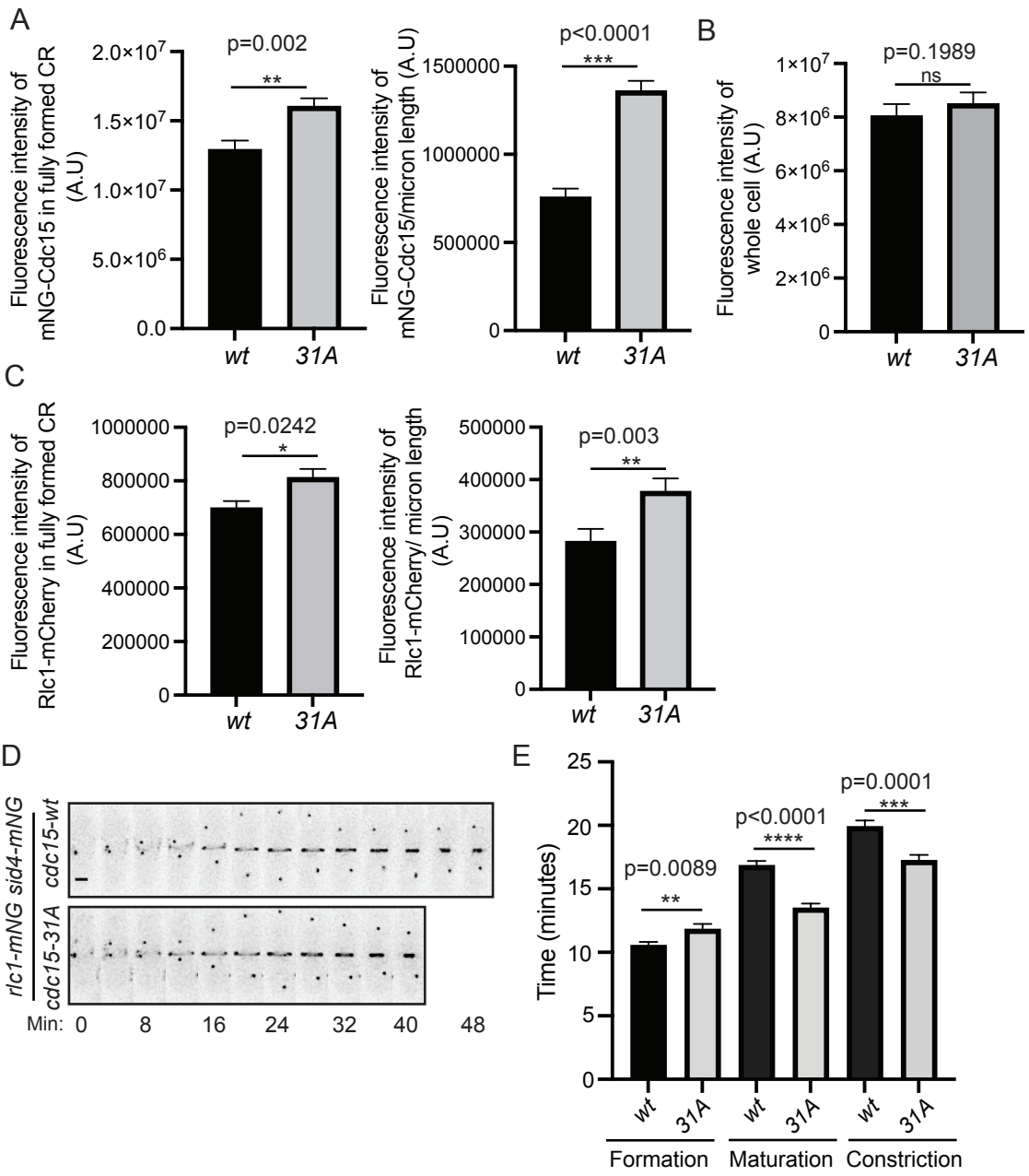

Figure 4

bioRxiv preprint doi: https://doi.org/10.1101/2022.08.26.505417; this version posted August 26, 2022. The copyright holder for this preprint (which was not certified by peer review) is the author/funder. All rights reserved. No reuse allowed without permission.

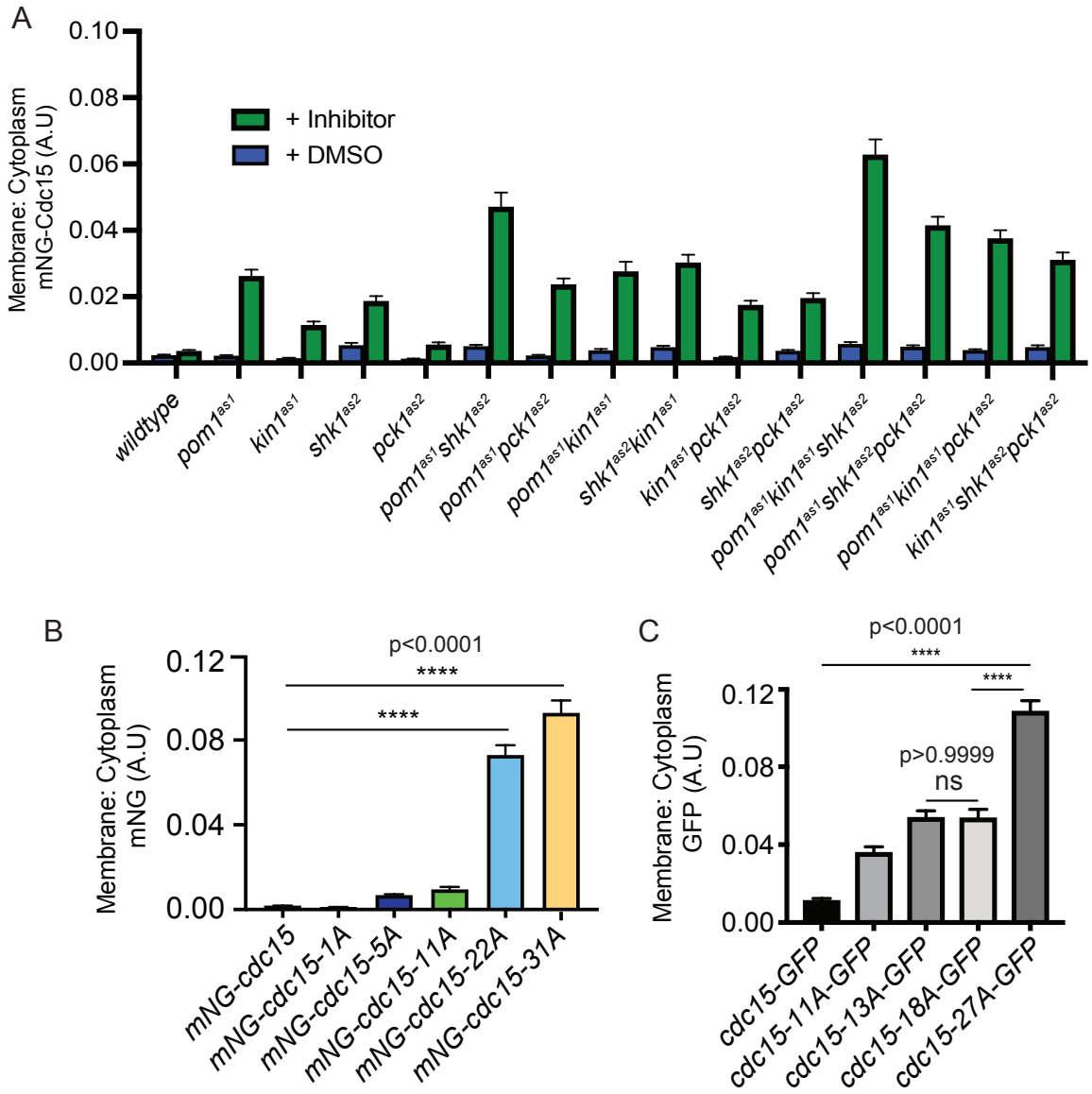

Figure 5

bioRxiv preprint doi: https://doi.org/10.1101/2022.08.26.505417; this version posted August 26, 2022. The copyright holder for this preprint (which was not certified by peer review) is the author/funder. All rights reserved. No reuse allowed without permission.

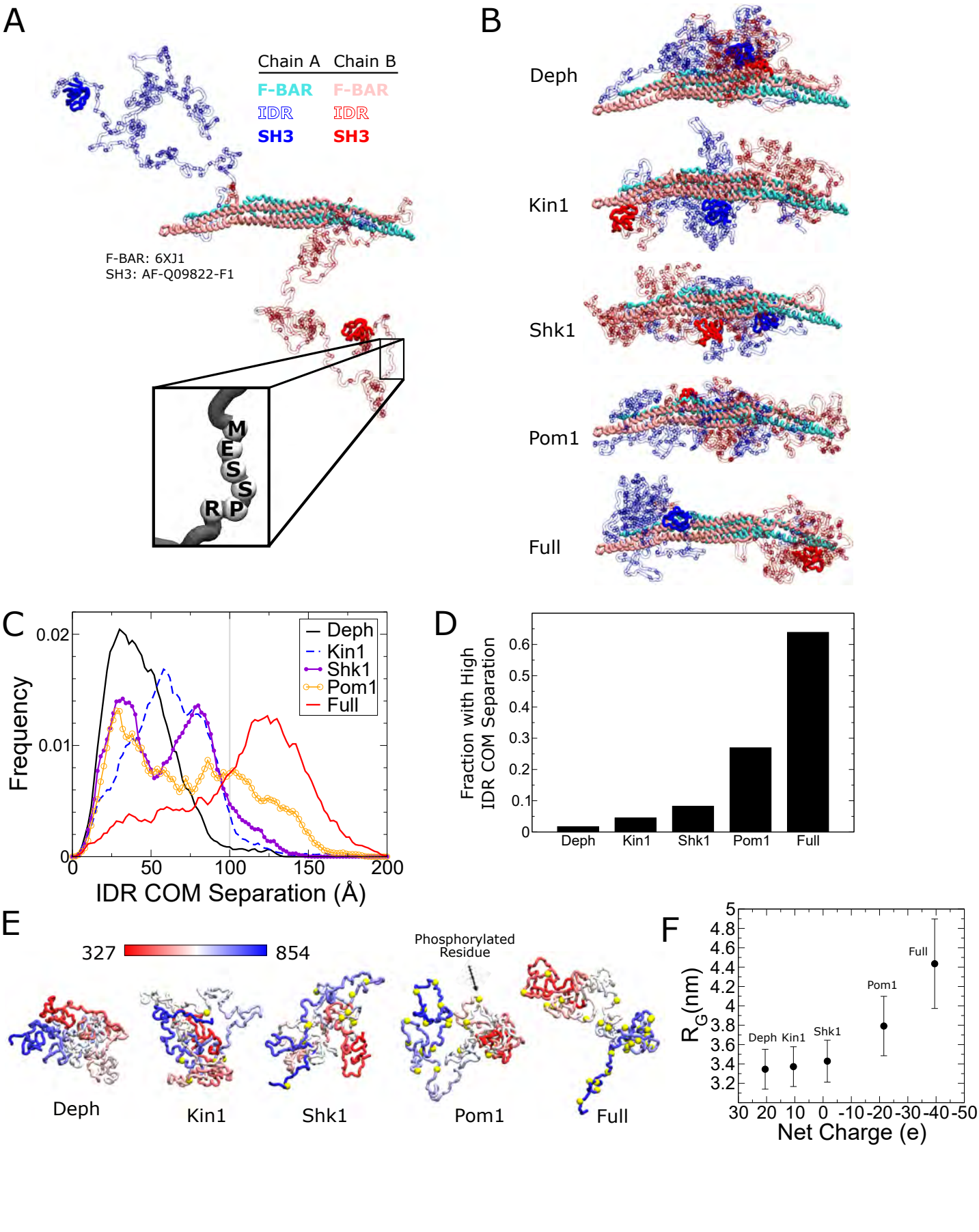

Figure 6

bioRxiv preprint doi: https://doi.org/10.1101/2022.08.26.505417; this version posted August 26, 2022. The copyright holder for this preprint (which was not certified by peer review) is the author/funder. All rights reserved. No reuse allowed without permission.

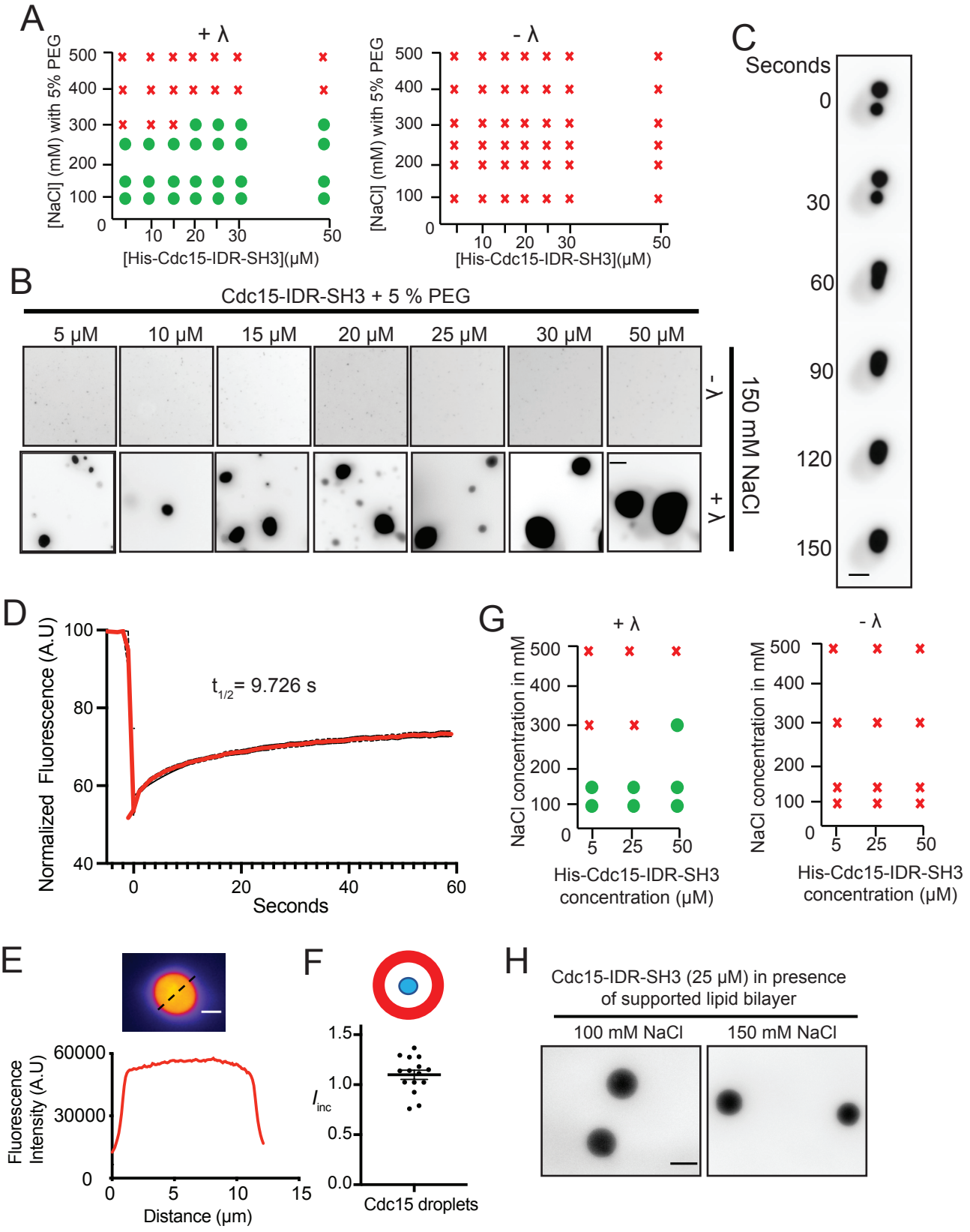

Figure 7

bioRxiv preprint doi: https://doi.org/10.1101/2022.08.26.505417; this version posted August 26, 2022. The copyright holder for this preprint (which was not certified by peer review) is the author/funder. All rights reserved. No reuse allowed without permission.

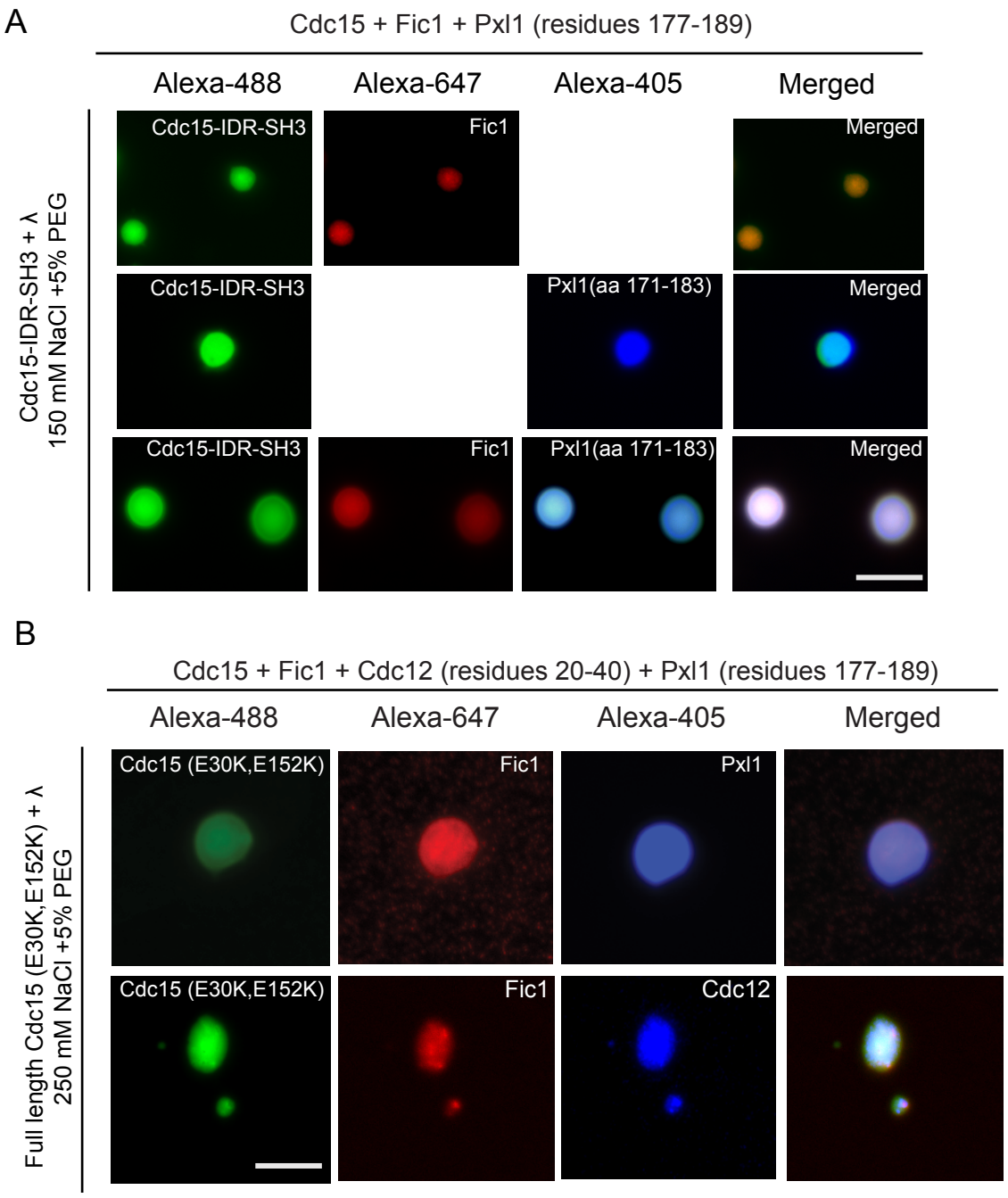

Figure 8

bioRxiv preprint doi: https://doi.org/10.1101/2022.08.26.505417; this version posted August 26, 2022. The copyright holder for this preprint (which was not certified by peer review) is the author/funder. All rights reserved. No reuse allowed without permission.

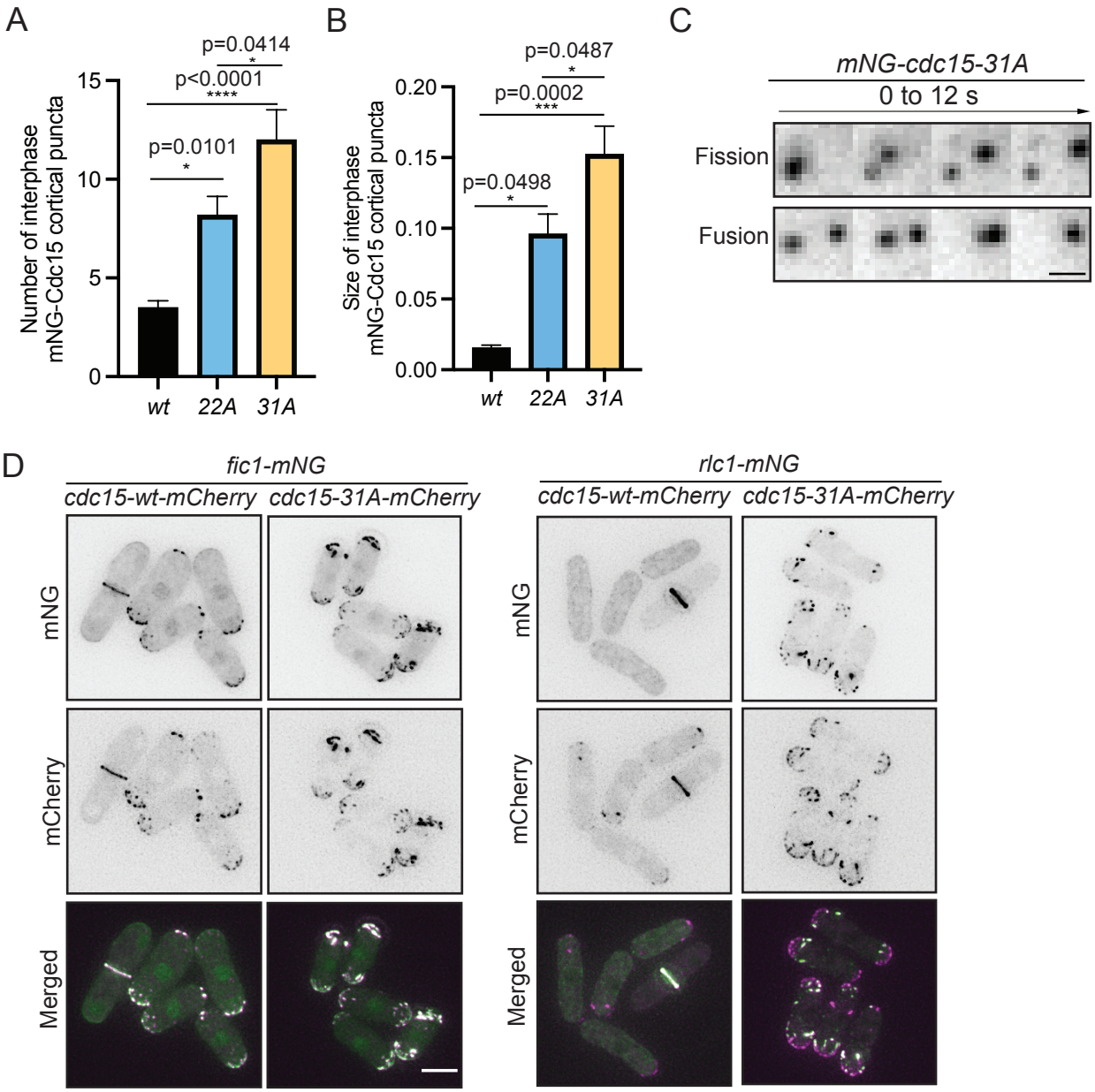

Figure 9